Department of Construction Sciences
Division of Solid Mechanics

ISRN LUTFD2/TFHF–12/5164-SE(1-74)

Experimental studies and modelling of pressboard

Master's thesis by
Jonas Engqvist

SUPERVISOR
DOCENT MATHIAS WALLIN, DIV. OF SOLID MECHANICS
PH.D. PER HÅRD AF SEGERSTAD, ABB CORPORATE RESEARCH

EXAMINER
PROF. MATTI RISTINMAA, DIV. OF SOLID MECHANICS

Printed by Media-Tryck, Lund ,Sweden

For information, address:
Division of Solid Mechanics, Lund University, Box 118, SE-221 00 Lund, Sweden.
Homepage: http://www.solid.lth.se

Preface

This Master's thesis has been carried out during the fall and winter of 2011 and the very beginning of 2012 at the Division of Solid Mechanics at Lund Institute of Technology (LTH), the technical faculty at Lund University. The work was proposed by ABB Corporate Research.

This work was initiated by Ph.D. Per Hård af Segerstad, ABB Corporate Research, whom also has been supporting through out the entire work. I would especially like to express my gratitude to my supervisor Docent Mathias Wallin for great amounts of valuable advises and without whom this Mater's thesis would not have been such an enjoyable experience.

I would also like to thank technician Zivorad Zivkovic at LTH for a help and advises during my experiments. My girlfriend must have a special thank for all her patience and support during the periods when I spend most of my awaken time inside the red brick buildings of LTH.

Just as my brother I would finally like to thank the coffee makers of South America without which this work never had been possible.

Abstract

To ensure that a power transformer can be operated after, e.g, a short circuit it is of most importance that the windings in the transformer are kept in place. To be able to simulate the preprocessing of the material, pressboard, that keeps the windings in place one has to have knowledge about how the material behaves during loading. Secondly one needs a constitutive model that can describe the material behaviour.

Within this Master's thesis some uniaxial tensile and compression tests have been made that shows some fundamental behaviours of pressboard such as anisotropy and viscous effects. During the experimental work some difficulties were discovered such as increasing moisture and initial curvature of the material. Experiments describing stress relaxation during compression made at ABB is also used within the thesis.

A constitutive model based on Norton creep that captures the behaviour of the material is proposed and fitted to the experimental data. The model is implemented in a FE-code into Matlab and derivations of the stress and algorithmic tangent stiffness are provided. The thesis is finalised by implementing the model as an user material subroutine to Abaqus/Standard.

Contents

1 Introduction

In this section the objective and restictions of this Master's thesis are presented along with a short introduction of ABB and the material pressboard. Some fundamental notations and definitions are also presented in this section.

1.1 Presentation of ABB

ABB is a global power and automation company with about 130,000 employees in about 100 countries. ABB was formed in 1988 when the Swedish company ASEA and the Swiss company BBC - Brown Boveri merged. ASEA dates back to 1883 when Ludvig Fredholm established Elektriska Aktiebolaget in Stockholm which manufactured electrical lighting and generators.

ABB Corporate Research has seven research centres around the world, one of which are located in Västerås in Sweden. ABB Power Products and Power Systems develop and manufacture components to transmit and distribute electric energy such as power transformers, circuit breakers and high-voltage cables. In the line of products there are components both for high-voltage alternating current and high-voltage direct current.

1.2 Thesis objective

To ensure that a power transformer can be operated after, e.g., a short circuit it is of utmost importance that the windings in the transformer are kept in place. This is achieved by preloading the components that keeps the windings in place in the transformer. In some ABB power transformers the components that keeps the windings in place are fabricated in the material *pressboard*. The ability to keep the windings in place is determined by how the material is preloaded in the assembly process of the transformer. To be able to simulate the preloading procedure in order to improve the ability to keep the windings in place one first has to have some knowledge about how the material behaves during loading, and how the stress in the material varies over time when the deformation is fixed. Secondly one needs a constitutive model that predicts the behaviour accurately enough to ensure correlation between the results from the simulation and the reality.

The objective with this thesis is essential divided into two parts. The first is to get more knowledge about the behaviour of pressboard during loading by performing uniaxial tensile and compression tests. The second part is to propose a constitutive model that describes the behaviour found by the experiments made within the Master's thesis and stress relaxation experiments made at ABB. The constitutive model is implement in a finite

element code in Matlab and as an umat-subroutine[1] into the commercial finite element software Abaqus.

1.3 Restrictions

The experiments made within the thesis are restricted to uniaxial tensile and compression tests, mainly because of lack of equipment. The modelling is restricted to small deformation. This is because of that a large deformation model would require more time than what is available within the frame of this Master's thesis.

Due to secrecy some parts of this thesis are omitted. This explains, e.g., the absence of numerical values of the model parameters as well as normalized values of the axes and time periods in some parts of this thesis.

1.4 Pressboard

Pressboard is a cellulose material used as solid insulation, primarily in oil filled power transformers with a voltage range from hundreds of volt upto over 1000 kV. Cellulose is a polymer consisting of glucose chains which are obtained from wood. Through a series of chemical processes the wood is decomposed into pulp. The pulp also contains other polymers which are removed from the finished pulp which is carefully washed in order to decrease the electric conductivity. The finished pulp is then fed onto a moving mesh and formed and dried in a press, cf. [1]. Through the manufacturing process the material obtains orthotropic properties. This means that the material possesses different properties in three orthogonal directions. These directions are commonly known as, Machine direction (MD), Cross machine direction (CD) and Z direction (Z). In this thesis the direction are sometimes referred to as (1), (2) and (3) respectively. The machine direction are the direction in which the pressboard has been produced, the cross machine direction are orthogonal to MD in the pressboard plane and the Z direction are normal to the pressboard plane, cf. figure 1.1.

1.5 Definitions and notations

1.5.1 Notations

In this thesis two different notations are used, namely *matrix notation* and *index notation*. *Cartesian coordinate system* is used through out the thesis.

[1] umat - user-defined material behaviour

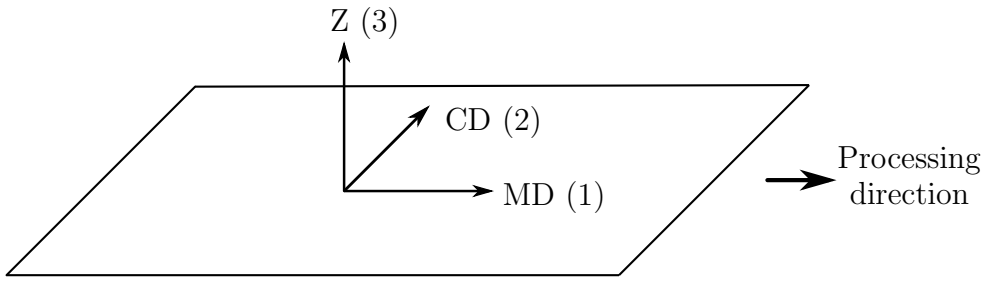

Figure 1.1: The figure are showing the three material directions of pressboard.

The matrix notation uses bold letters indicating vectors and matrices

$$\boldsymbol{a} = \begin{bmatrix} a_1 \\ a_2 \\ a_3 \end{bmatrix}, \quad \boldsymbol{B} = \begin{bmatrix} B_{11} & B_{12} & B_{13} \\ B_{21} & B_{22} & B_{23} \\ B_{31} & B_{32} & B_{33} \end{bmatrix} \tag{1.1}$$

Using index notation the vector $\boldsymbol{a}$ can be written as a_i where the index i takes the value 1,2 and 3. It is also possible to use more than one index. The matrix $\boldsymbol{B}$ can as an example be written as B_{ij} where both indexes i and j takes the value 1 to 3. When using index notation there are a few important conventions. One is the *summation convention* which states that if the same index is used twice a summation over the index is implied. Let a_i and b_i be two column vectors with $i = 1, 2, 3$ then the summation convention states

$$a_i b_i = a_1 b_1 + a_2 b_2 + a_3 b_3 \tag{1.2}$$

The trace of the matrix $\boldsymbol{B}$ is in this manner written as B_{kk}

$$B_{kk} = B_{11} + B_{22} + B_{33} \tag{1.3}$$

If the same index is used twice it is called a *dummy* index and if it used once it is called a *free* index. An index can only be a free or a dummy index. An other important convention is the *comma convention* that is used to indicate differentiation with a comma, i.e.

$$\frac{\partial f}{\partial x_i} = f_{,i} \quad \frac{\partial u_i}{\partial x_j} = u_{i,j} \tag{1.4}$$

A very important function when dealing with index notion is the *Kronecker delta* δ_{ij} defined as

$$\delta_{ij} = \begin{cases} 1 & if \quad i = j \\ 0 & if \quad i \neq j \end{cases} \tag{1.5}$$

Using the summation convention it follows that

$$B_{ij}\delta_{jk} = B_{ik} \tag{1.6}$$

1.5.2 Strain tensor

The strain tensor is defined as, cf. [2]

$$E_{ij} = \frac{1}{2}\left(\frac{\partial u_i}{\partial X_j} + \frac{\partial u_j}{\partial X_i} + \frac{\partial u_k}{\partial X_i}\frac{\partial u_k}{\partial X_j}\right) \tag{1.7}$$

where u_i is the displacement vector describing how of a material point displaces from the position X_i in the reference configuration before the deformation to the position x_i after the deformation. Using the comma convention the strain tensor can be written as

$$E_{ij} = \frac{1}{2}(u_{i,j} + u_{j,i} + u_{k,i}u_{k,j}) \tag{1.8}$$

The strain tensor is sometimes called *Green's strain tensor*. The strain tensor is a symmetric second order tensor. When, as in this thesis, considering small displacements the displacement gradient $u_{i,j}$ are small when compared to unity. As a consequence of this the quadratic term in (1.8) can be ignored and E_{ij} can be approximated by the small strain tensor ε_{ij} defined by

$$\varepsilon_{ij} = \frac{1}{2}(u_{i,j} + u_{j,i}) \tag{1.9}$$

The *relative elongation* or *engineering strain*, ε defined as

$$\varepsilon = \frac{\Delta l}{l_0} \tag{1.10}$$

where Δl is the elongation and l_0 is the initial length.

1.5.3 Stress tensor

The stress tensor is defined as

$$[\sigma_{ij}] = \begin{bmatrix} \boldsymbol{t}_1^T \\ \boldsymbol{t}_2^T \\ \boldsymbol{t}_3^T \end{bmatrix} = \begin{bmatrix} \sigma_{11} & \sigma_{12} & \sigma_{13} \\ \sigma_{21} & \sigma_{22} & \sigma_{23} \\ \sigma_{31} & \sigma_{32} & \sigma_{33} \end{bmatrix} \tag{1.11}$$

where $\boldsymbol{t}_1$, $\boldsymbol{t}_2$ and $\boldsymbol{t}_3$ are components of the traction vector in the x_1, x_2 and x_3 directions respectively. The traction vector is defined as

$$\boldsymbol{t} = \lim_{\Delta A \to 0} \frac{\Delta \boldsymbol{P}}{\Delta A}; \qquad \boldsymbol{t} = \begin{bmatrix} \boldsymbol{t}_1 \\ \boldsymbol{t}_2 \\ \boldsymbol{t}_3 \end{bmatrix} \tag{1.12}$$

where ΔA is an incremental surface area with the outward directed unit normal vector $\boldsymbol{n}$ and $\Delta \boldsymbol{P}$ are an incremental force vector, see figure 1.2.

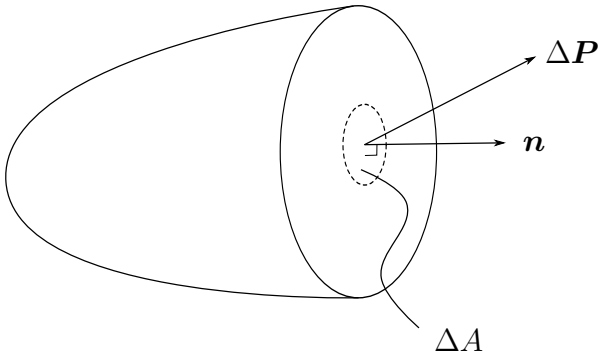

Figure 1.2: incremental force vector $\Delta \boldsymbol{P}$ acting on the incremental surface area ΔA with the outward directed unit normal vector $\boldsymbol{n}$.

In the same fashion as for the engineering strain the *engineering stress* is defined as

$$\sigma = \frac{F}{A_0} \tag{1.13}$$

where F is the normal force acting on the surface and A_0 is the initial area.

2 Experiments

In this section the experiments made within this thesis are presented along with experiments made at ABB.

2.1 Introduction

To be able to understand the behaviour of the material it is necessary to preform material testing. A great deal of time and effort had to be devoted to experiments due to lack of material data of pressboard in the literature. Experiments were made at LTH during the spring and summer of 2011. These experiments were uniaxial tensile and compression test with short duration. The experiments and its results are presented in section 2.3 to 2.6. During the late summer of 2011 uniaxial relaxation experiments were provided by ABB. These experiments and its results are presented in section 2.7.

All the tests made at LTH were made using a Instron 8500 tensile test machine with a MTS 250 kN load cell. During the tensile tests the strain were measured using an Instron 2620 extensometer which was attached to the specimen using rubber O-rings. The gauge length of the extensometer were 12.5 mm for the initial experiments and 25 mm for the later experiments. During the compression tests the strain was measured using the test machines builtin measuring system. Figure 2.1 is showing the machine set-up for the tensile tests and figure 2.2 the set-up for the compression tests. The temperature and the humidity of the air was measured during all the tests. The average temperature was 23 ± 2 °C and the average humidity was $65 \pm 10\%$.

2.2 Material

The specimens used for the tensile tests was rectangular bars with the dimensions 400 mm × 15 mm and a thickness of 3 mm. These were cut into three equally large pieces with the dimensions 133 mm × 15 mm. Three sets of specimens were supplied: in the MD-, CD-direction and 45° to the MD-direction. For the compression test, 3 mm and 8 mm thick square pieces were used. The 3 mm thick pieces measured 25 mm × 25 mm and the 8 mm 26 mm × 26 mm. The actual size of every specimen were measured before the test using a micrometer. All the specimens were delivered wrapped in plastic (in which they also were stored until the tests were made) and contained about 2% moisture when leaving the supplier. Because of that the duration of each test was relatively short (less than 5 minutes) the specimens

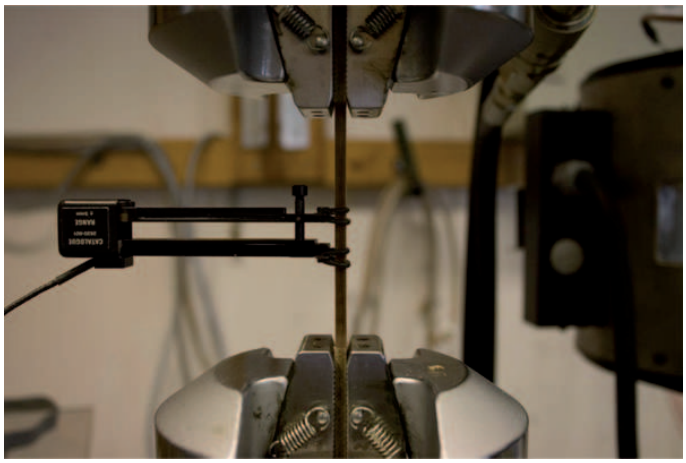

Figure 2.1: The picture shows a specimen with a milled down middle part in the tensile testing machine. The extensometer attached to the specimen is also shown in the figure.

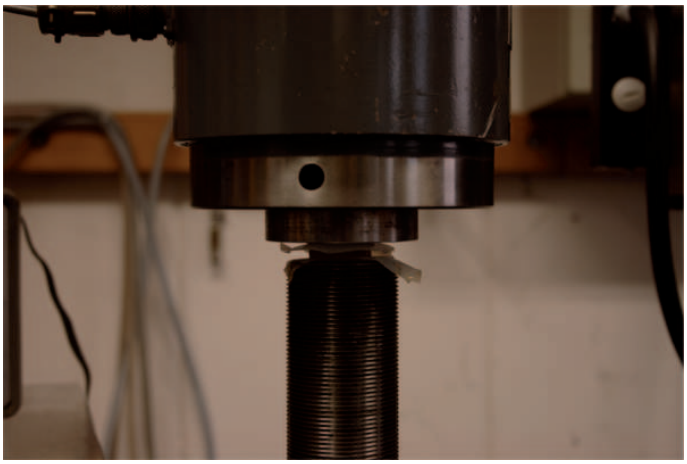

Figure 2.2: The picture is showing the machine set-up for the uniaxial compression tests with a 8 mm specimen.

was not wrapped in plastic during the tests, even though the air humidity was relatively high.

2.3 Effects of moisture

After some testing with a large scatter between the results it was discovered that the moisture content of the material probably increase even when the pieces were stored wrapped in plastic. Because of this the specimens were dried in a ventilated oven at 105°C, following the norm IEC 60641-2, before

testing, cf. [3]. The specimens with a thickness of 3 mm were dried for at least 48 hours and the 8 mm thick pieces for at least 72 hours. The drying did not only result in that the spread between the tests decreased to some extend. It did also result in that the stiffness of the material increased, see figure 2.3.

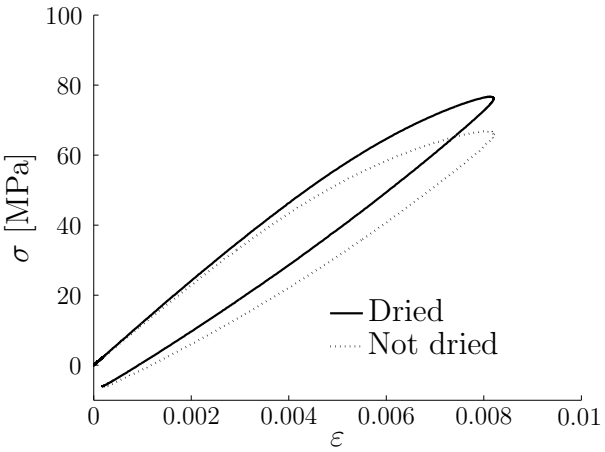

Figure 2.3: The graph is showing how the moisture content of the material affects the stiffness. The sample labeled "Not dried" were stored wrapped in plastic but not dried after delivery. These tests were made using a sinus shaped strain controlled loading curve with a constant frequency of 0.1 Hz. The gauge length of the extensometer were 25 mm during these tests.

2.4 Initial curvature

At about the same time as the problem with the increasing moisture was detected it was also discovered that the specimens were slightly curved when delivered. A set of tensile tests were made to examine the effect of the initial curvature of the specimens. The test were preformed by loading and unloading a dried specimen inside the elastic region while measuring the strain with the extensometer on the "inside" of the curvature. Then the extensometer were moved to the "outside" of the curvature and a new loading/unloading cycle were preformed. This procedure were repeated three times with the same specimen. Figure 2.4 illustrates the "inside"/"outside" placement of the extensometer on the bent specimen. The test showed that the strain differed between the two sides of the specimen due to the initial curvature, see figure 2.5. The figure is showing the mean value of three tests per side. The complete serie of results are found in appendix A.2. The test were performed

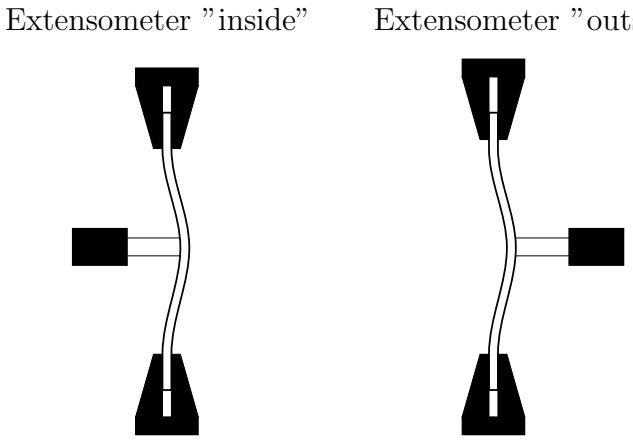

Figure 2.4: The figure illustrates the "inside"/"outside" placement of the extensomter on the curved specimen. The curvature of the specimen is grossly enlarged in the figure.

with a sinus shaped loading curve with a constant frequency of 0.1 Hz. The extensometer gauge length were 25 mm for this test.

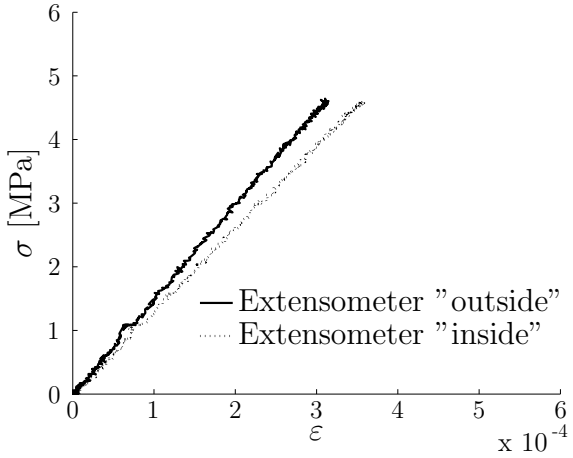

Figure 2.5: The graph illustrating the strain difference between the two sides of the specimen due to the initial curvature. The tests were performed using a sinus shaped loading curve with a constant frequency of 0.1 Hz. The specimen were dried before the test.

Attempts to correct the curvature were made in the subsequent tests. But due to the fact that an stress state is introduced in the specimen when it is straightened out the initial curvature affects the result of the tests. Due to the remaining spread even after the drying and the correction of the curvature all the graphs showing experimental data in this report is showing the mean value of several tests unless otherwise stated. The results of which the mean value were calculated is found in appendix A.

2.5 Uniaxial tensile tests

2.5.1 Loading until fracture

To be able to estimate how much the specimens could be loaded without breaking a first set of uniaxial tensile tests were carried out where the pieces were loaded with a constant displacement rate of 0.1 mm/s until fracture. To make sure that the specimens did not break in the mounting points the middle part of the pieces where milled down to a width of 10 mm for this set of tests. During these tests the extensometer gauge length were 12.5 mm. Figure 2.6 is showing the stress-strain curves for the three different directions and how the stiffness differs between the directions. Every curve is showing the mean value of five samples. The specimens used in this test were neither dried nor straightened out. Due to some spread between the fracture point of the different samples the curves are truncated.

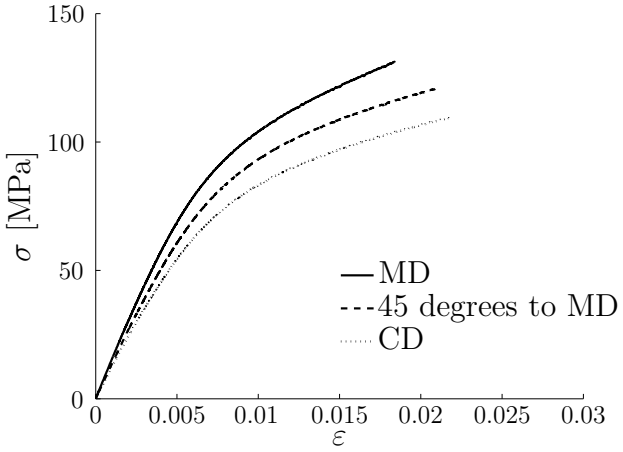

Figure 2.6: Uniaxial stress-stain curves for loading until fracture with a constant rate of displacement of 0.1 mm/s in the MD-, CD-direction and 45 degrees to the MD-direction. Every curve is showing the mean value of five specimens. The specimens were not dried before the test.

2.5.2 Cyclic tensile testing

To get as much information as possible out of each tensile test a series of tests with load controlled cyclic loading/unloading were carried out. The tests were carried out by loading the specimen up to six different load levels from 1.1 to 3.6 kN in steps of 0.5 kN. Between every load level the piece was unloaded. To make sure that the specimen not were subjected to compression the unloading was stopped at 0.1 kN. The first sets of cyclic tests were carried out with a triangular formed loading curve. After some testing it was discovered that the test machine did not operate accurate enough when the loading direction were changed. The consequence of this was that all the load cycles did not start and stop at the same force level which lead to an increase of the scatter between the cycles. This because the pieces had a different amount of inelastic strains when loaded to different load levels and did not unload to the same strain levels. This was solved using a sinus shaped loading curve with a constant frequency of 0.1 Hz. During these tests an extensometer with a gauge length of 12.5 mm were used. Figure 2.7 is showing the stress-strain curve in the three different directions using the sinus shaped cyclic loading curve. The specimens used in these tests were neither dried nor straightened out.

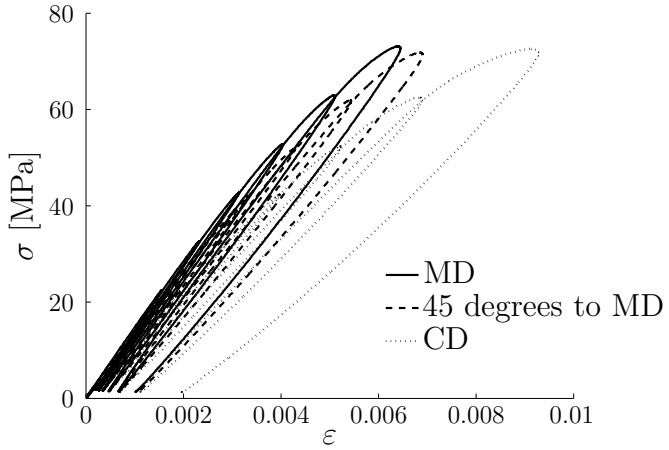

Figure 2.7: Uniaxial stress-strain curve with load controlled cyclic loading/unloading. Every curve is showing the mean value of six specimens.The specimens were not dried or straightened out before the test. The specimens were loaded using a sinus shaped loading curve with a constant frequency of 0.1 Hz.

2.5.3 Strain controlled loading

Due to problems with a relatively large scatter between the tests the cyclic loading curve was later replaced with a strain controlled curve with only one loading/unloading cycle. The shape of the strain curve were kept as a sinus shaped loading curve with a constant frequency of 0.1 Hz. This decreased the scatter between the tests, especially around the point where the loading changed direction. But even with strain controlled loading there were some scatter even in elastic region. Figure 2.8 is showing the result from a strain controlled test series. Each curve is showing a mean value of nine tests. The error bars on the stress-strain curve in the MD-direction indicates the standard deviation from the average curve of the experimental data. The complete experimental data is found in appendix A.5. The specimens used in this test were dried and straightened out and the extensometer gauge length were 25 mm during these tests.

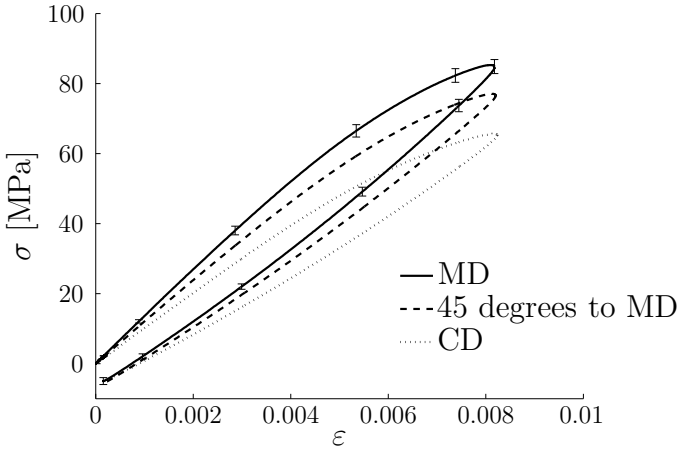

Figure 2.8: Uniaxial stress-strain curve with strain controlled loading and unloading. Every curve is showing the mean value of nine specimens. The error bars on the stress-strain curve in the MD-direction indicates the standard deviation from the average curve of the experimental data. The specimens were dried and straightened out before the test. The specimens were loaded using a sinus shaped strain curve with a constant frequency of 0.1 Hz.

2.6 Uniaxial compression tests made at LTH

A very limited series of uniaxial compression tests were made at LTH before receiving test data from compression tests made at ABB. The tests were made using a triangular loading/unloading curve with three different constant loading rates: 0.5, 20 and 40 kN/s. Between the loading and unloading the load was fixed for 1.0 second. Every test were made using a single square specimen which were compressed in the Z-direction. specimens with a thickness of 3 mm and 8 mm were used. The 3 mm thick pieces measured 25 mm $\times$ 25 mm and the 8 mm 26 mm $\times$ 26 mm. All specimens were dried before testing. Teflon film was used between the specimen and the compression platens on the machine to lower the friction. Figure 2.9 illustrates the machine set-up for the compression tests. To correct for the deformation of

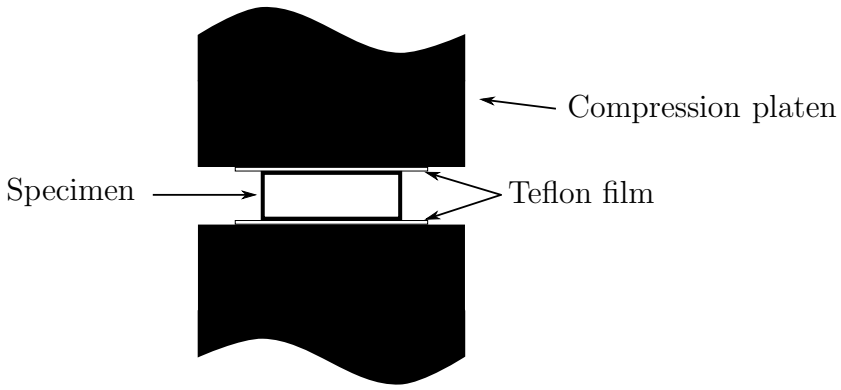

Figure 2.9: The figure illustrates the machine set-up for the compression tests made at LTH.

the machine one test without a specimen were made at every loading rate. The deformation from this test was deducted from the result with a specimen. Figure 2.10 and 2.11 are showing the results from the compression tests using 3 mm and 8 mm thick specimens respectively. These curves are showing the actual test results and not a mean value. Because of some laterally scattering the stress-stain curves are displaced so that the curves are connected when the compression force are -5.0 kN (which is equivalent to -8.0 MPa for the 3 mm thick pieces and -7.4 MPa for the 8 mm thick pieces). The spread is mostly due to some variation of the thickness of the specimens.

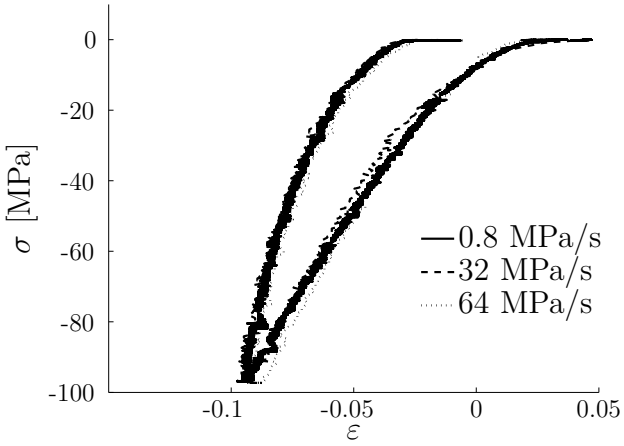

Figure 2.10: Uniaxial compression stress-strain curve using 3 mm thick square specimen. The specimens were dried before the test. Because of some laterally scatter the stress-stain curves are displaced so that the curves are connected when the pressure are -8.0 MPa. The scatter is mostly due to some variation of the thickness of the specimens. The curves are showing the actual test results and not a mean value.

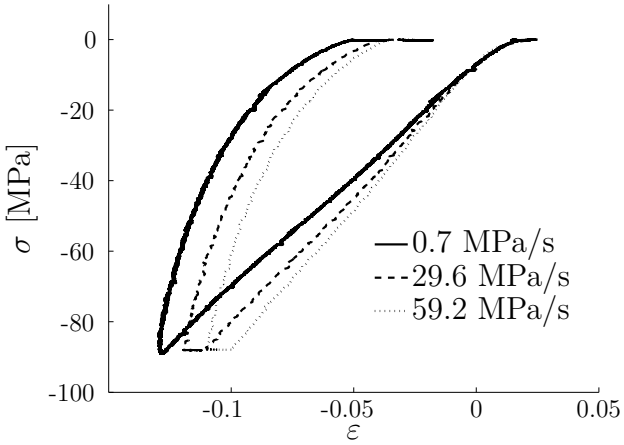

Figure 2.11: Uniaxial compression stress-strain curve using 8 mm thick square specimen. The specimens were dried before the test. Because of some laterally scatter the stress-stain curves are displaced so that the curves are connected when the pressure are -7.4 MPa. The scatter is mostly due to some variation of the thickness of the specimens. The curves are showing the actual test results and not a mean value.

2.7 Compression tests made at ABB

The results in this section is from compression tests made at ABB. The compression tests were made with stacks of several rectangular specimens. Before the tests the samples were dried. After the drying the stacks were wrapped in plastic. Every test were made with a new set of specimens.

2.7.1 Constant pressure before relaxation test

Tests were made where a constant pressure were applied to the test stack for five different time intervals before locking the height. The stress were recorded during a relaxation period with the duration t_0. Figure 2.12 is showing the result of the tests. The results are showing how the stress relaxation is decreasing when a constant pressure is applied before the height is fixed.

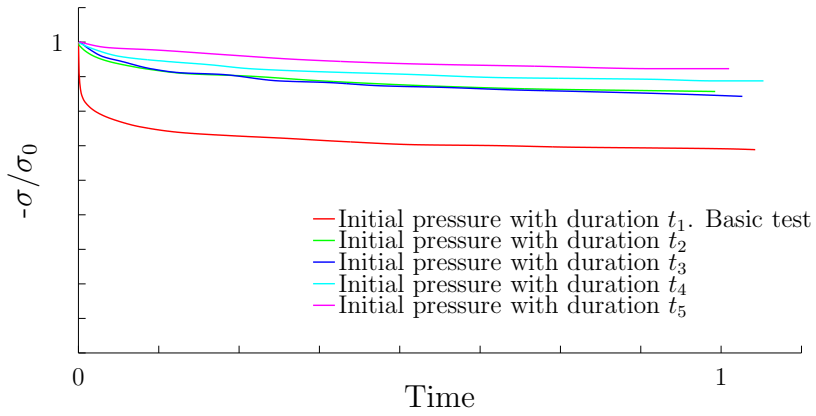

Figure 2.12: The graph is showing how the stress decreases with time when a constant pressure has been applied for five different lengths of time before the height were locked. Notice that the stress axis has been normalized using the normalization stress σ_0. The time axis is also normalized.

2.7.2 Repeated compression

Two sets of tests were made where the same test stack were compressed repeatedly with a period of unloading in between. During the first test the stack were pressed three cycles of t_6 constant height with t_7 without any load in between. The result is showed in figure 2.13. The second test were made with three cycles of t_8 constant height with t_9 rest in between. This test were ended with one cycle after the time t_{10} without any load. The result of these

tests is showed in figure 2.14. The results is showing the stress relaxation decreases after every cycle.

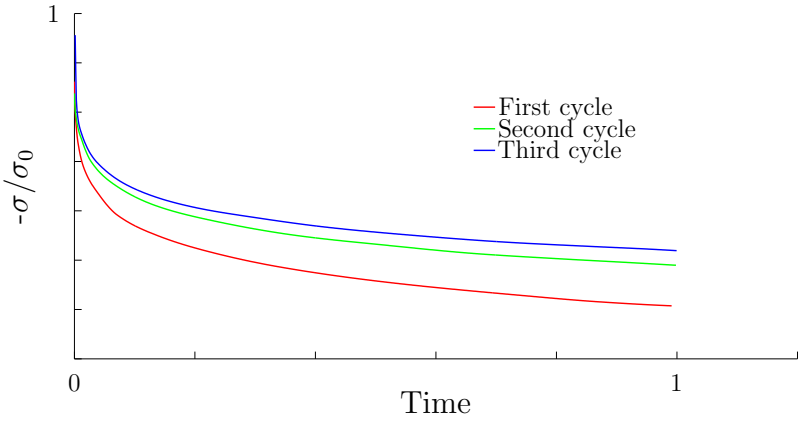

Figure 2.13: The graph shows how the stress decreases with time when the test stack has been compressed repeatedly. The test consisted of three cycles of t_6 constant height with t_7 rest in between. Notice that the stress axis has been normalized using the normalization stress σ_0. The time axis is also normalized.

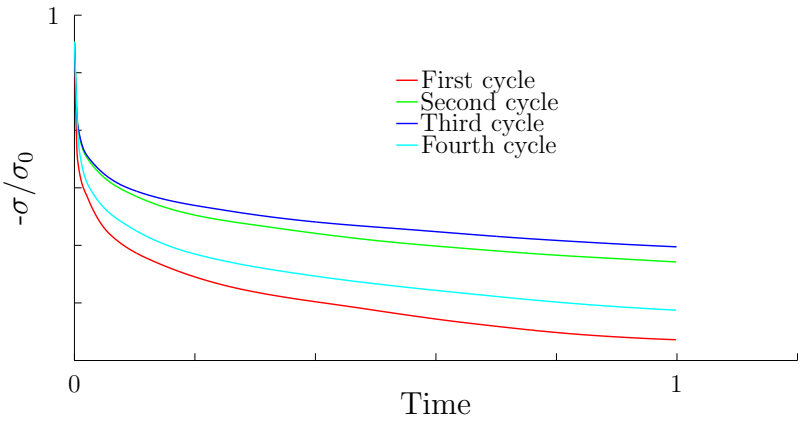

Figure 2.14: The graph shows how the stress decreases with time when the test stack has been compressed repeatedly. The test consisted of three cycles of t_8 constant height with t_9 rest in between. One final cycle were made after a rest period of t_{10}. Notice that the stress axis has been normalized using the normalization stress σ_0. The time axis is also normalized.

3 One dimensional model

In order to determine which type of constitutive model that were needed to predict the behaviour of the material, revealed in the experiments a couple of different one-dimensional models were implemented in Matlab. Emphasis was on the compression experiments made at ABB, presented in section 2.7. The constitutive equations were expressed on time-rate format and integrated in Matlab using an ODE (ordinary differential equation) solver. Figure 3.1 illustrates the final constitutive model, consisting of three linear springs and two non-linear dashpots. In this section the theory behind the one-dimensional model is presented as well as the Matlab implementation, the procedure used to determine model parameters and results from the model compared with experimental data.

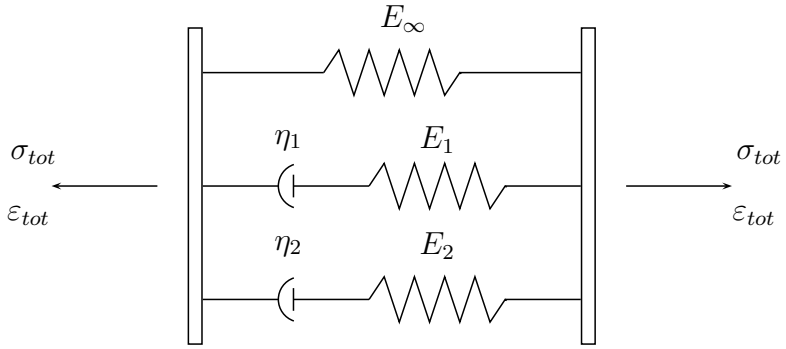

Figure 3.1: The figure is showing the final constitutive model consisting of three linear springs and two non-linear dashpots.

3.1 Theory

The linear springs were modelled according to Hooke's law. In time-rate format Hooke's law in one dimension can be written as equation (3.1) where the superscript e refer to the elastic behaviour. The non-linear dashpots were modelled using Norton's power creep law, see equation (3.2) where the superscript cr refer to the creep response, cf. [2].

$$\dot{\varepsilon}^e = \frac{\dot{\sigma}^e}{E} \tag{3.1}$$

$$\dot{\varepsilon}^{cr} = sign(\sigma)\left(\frac{|\sigma|}{\sigma_0}\right)^m \tag{3.2}$$

When two elements are in series (figure 3.2) the total strain rate and stress of the two elements is

$$\dot{\varepsilon} = \dot{\varepsilon}^e + \dot{\varepsilon}^{cr}; \qquad \sigma = \sigma^e = \sigma^{cr}$$

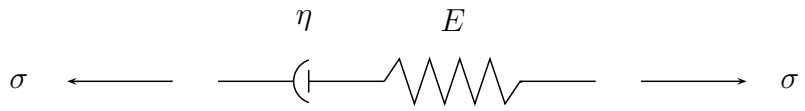

Figure 3.2: Two elements in series

When two elements are in parallel (figure 3.3) the total strain rate and stress of the two elements is

$$\dot{\varepsilon} = \dot{\varepsilon}^e = \dot{\varepsilon}^{cr}; \qquad \sigma = \sigma^e + \sigma^{cr}$$

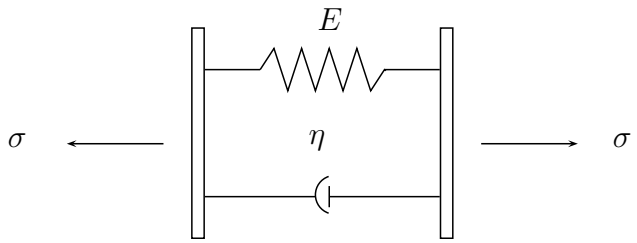

Figure 3.3: Two elements in parallel

Using this together with equations (3.1) and (3.2) the stress rates for the model illustrated in figure 3.1 can be written as

$$\begin{cases} \dot{\sigma}_\infty &= E_\infty \dot{\varepsilon}_{tot} \\ \dot{\sigma}_1 &= E_1 \left(\dot{\varepsilon}_{tot} - sign(\sigma_1) \left(\dfrac{|\sigma_1|}{\sigma_{0_1}} \right)^{m_1} \right) \\ \dot{\sigma}_2 &= E_2 \left(\dot{\varepsilon}_{tot} - sign(\sigma_2) \left(\dfrac{|\sigma_2|}{\sigma_{0_2}} \right)^{m_2} \right) \end{cases} \tag{3.3}$$

The total stress rate is given as the sum of the three stress rates

$$\dot{\sigma}_{tot} = \dot{\sigma}_{\infty} + \dot{\sigma}_1 + \dot{\sigma}_2 \tag{3.4}$$

The initial response to a sudden load is pure elastic with the total stiffness of the sum of the stiffness of the three springs. This is because of that the dashpot responds as rigid elements to a suddenly applied load.

$$E_0 = E_{\infty} + E_1 + E_2 \tag{3.5}$$

3.2 Implementation

The constitutive equations (3.3) were integrated in Matlab using an ODE-solver. The implementation was made for two different load cases: prescribed total strain rate and prescribed total stress rate. Depending on the load case the expression for the total strain rate in (3.3) take different forms. These different forms are presented in box 3.1.

Box 3.1 Total strain rate depending on the load case

Load case:

1. Relaxation:

$$\dot{\varepsilon}_{tot} = 0$$

2. Creep and loading/unloading:

$$\dot{\varepsilon}_{tot} = \frac{1}{E_0}\left[\dot{\sigma}_{tot} + sign(\sigma_1)E_1\left(\frac{|\sigma_1|}{\sigma_{0_1}}\right)^{m_1} + sign(\sigma_2)E_2\left(\frac{|\sigma_2|}{\sigma_{0_2}}\right)^{m_2}\right]$$

   Creep $\Rightarrow \dot{\sigma}_{tot} = 0$

   Loading/unloading $\Rightarrow \dot{\sigma}_{tot} = constant \neq 0$

where E_0 is given by (3.5)

3.3 Parameters

The constitutive model stated in (3.3) contains seven parameters, presented in table 3.1. These were determined by curve fitting the model to the experimental data. This was made by calculating the stress during a load cycle equivalent to the experiment, e.g., loading from no stress up to the stress level used in the experiment followed a by relaxation period with the same

Table 3.1: Model parameters

E_∞	Linear elastic leg
E_1	Non-linear creep leg 1
σ_{0_1}	
m_1	
E_2	Non-linear creep leg 2
σ_{0_2}	
m_2	

duration as in the experiment. For the experiments involving a relaxation period the error was calculated as the difference between the stress from the experiment and the stress given by the model at N different points in time. For the force controlled uniaxial compression experiments the error was calculated as the difference between the strain from the experiment and the strain given by the model at N different stress levels. The number of test points N did differ between the different experiments. Using the least square method the error f were calculated as a sum of the square of the difference between the stress/strain given by the model and the stress/strain from experiments at N different points, cf. [4].

$$f = \sum_{i=1}^{N} \left(1 - \frac{\sigma_i^{exp}}{\sigma_i^{model}}\right)^2; \quad f = \sum_{i=1}^{N} \left(1 - \frac{\varepsilon_i^{exp}}{\varepsilon_i^{model}}\right)^2 \tag{3.6}$$

where superscript *model* denotes the stress/strain given by the model and *exp* denotes the stress/strain given by the experiments.

The experimental data used during the curve fitting procedure were all the data from the two experiments with repeated compression presented in section 2.7.2 and the long time relaxation experiment called "basic test" in figure 2.12, which is further described in section 2.7.1. The initial stiffness (3.5) were determined using the uniaxial compression test of a 8 mm thick test piece at a constant loading rate of 0.5 kN/s. The experiments are described in section 2.6.

3.4 Results

All the results presented in this section are produced using the same model and the same set of parameters. The figures are showing the results from the model compared with experimental data.

3.4.1 Initial stiffness

Figure 3.4 is showing the initial stress-strain curve from the model compared with experimental data for a uniaxial compression test. This curve were used in the curve fitting procedure to determine the model parameters in table 3.1.

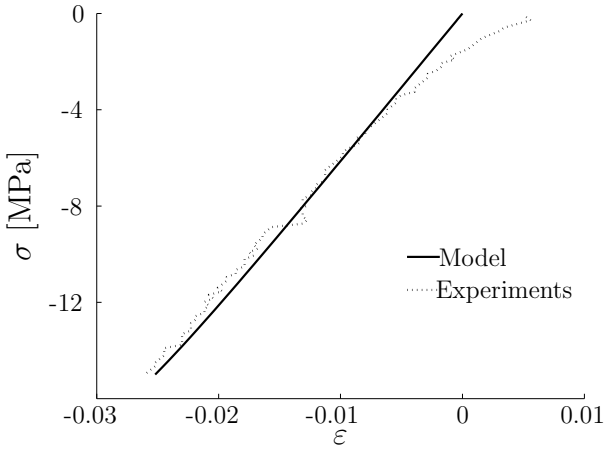

Figure 3.4: The graph is showing the initial stress-strain curve from the model compared with experimental data from a uniaxial compression test. This curve were used when determining the model parameters in table 3.1.

3.4.2 Repeated compression

Figure 3.5 is showing the results from the model with repeated compression and a rest period of t_9 in between the compression cycles. The fourth cycle (cycle d) was carried out after a recovery period of t_{10}. Figure 3.6 is showing the results from the model with repeated compression with a recovery period with the duration t_7 between the cycles. The experiments are further explained in section 2.7.2. All of the curves in figure 3.5 and 3.6 were used to determining the model parameters in table 3.1.

3.4.3 Constant pressure before relaxation test

Figure 3.7a is showing the result from the model compared to experimental data during a relaxation test with the duration t_0 where an initial pressure is applied and the height is fixed after loading during the time t_1. This curve were used when the model parameters in table 3.1 were determined. The figures 3.7b to 3.7e is showing the comparison between the result from the

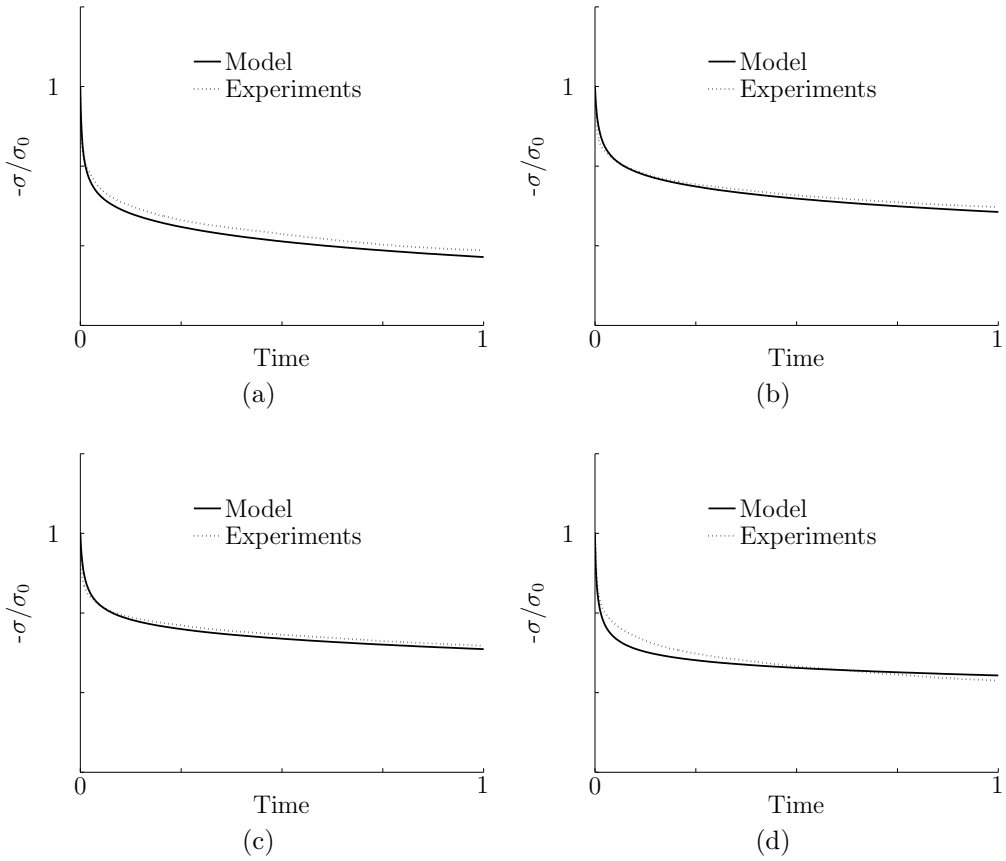

Figure 3.5: The graphs are showing results from the model compared with experimental data when the same test piece is exposed to repeated compression and relaxation. Graphs (a)-(c) is showing the first three cycles with a rest period with the duration t_9 between the cycles. Cycle (d) was carried out after a recovery period with the duration t_{10}. All four curves were used when the model parameters in table 3.1 were determined. Notice that the stress axis has been normalized using the normalization stress σ_0. The time axis is also normalized.

model and experimental data during t_0 relaxation tests where the initial pressure were held constant for the duration t_2, t_3, t_4 and t_5, respectively, before the height were fixed. These curves were not used when the model parameters in table 3.1 were determined. The experiments are further described in 2.7.1.

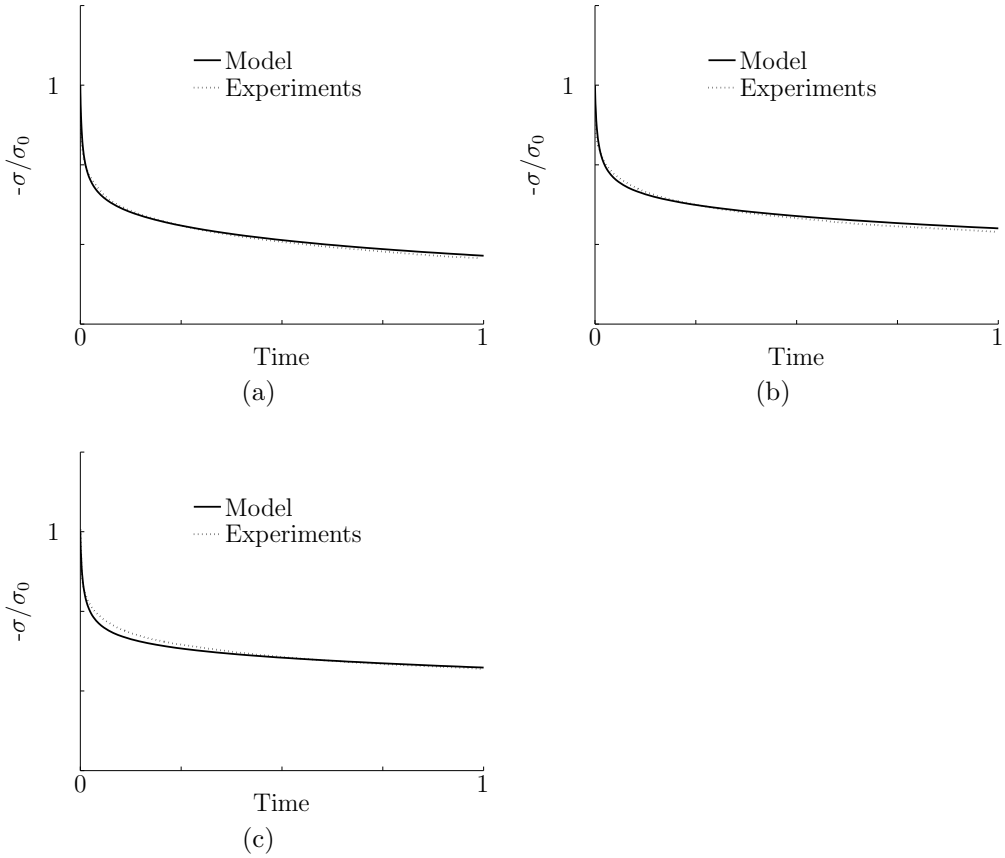

Figure 3.6: Results from the model compared with experimental data when the same test piece is exposed to repeated compression and relaxation. The test piece has recovered for t_7 between the cycles. All these curves were used when the model parameters in table 3.1 were determined. Notice that the stress axis has been normalized using the normalization stress σ_0. The time axis is also normalized.

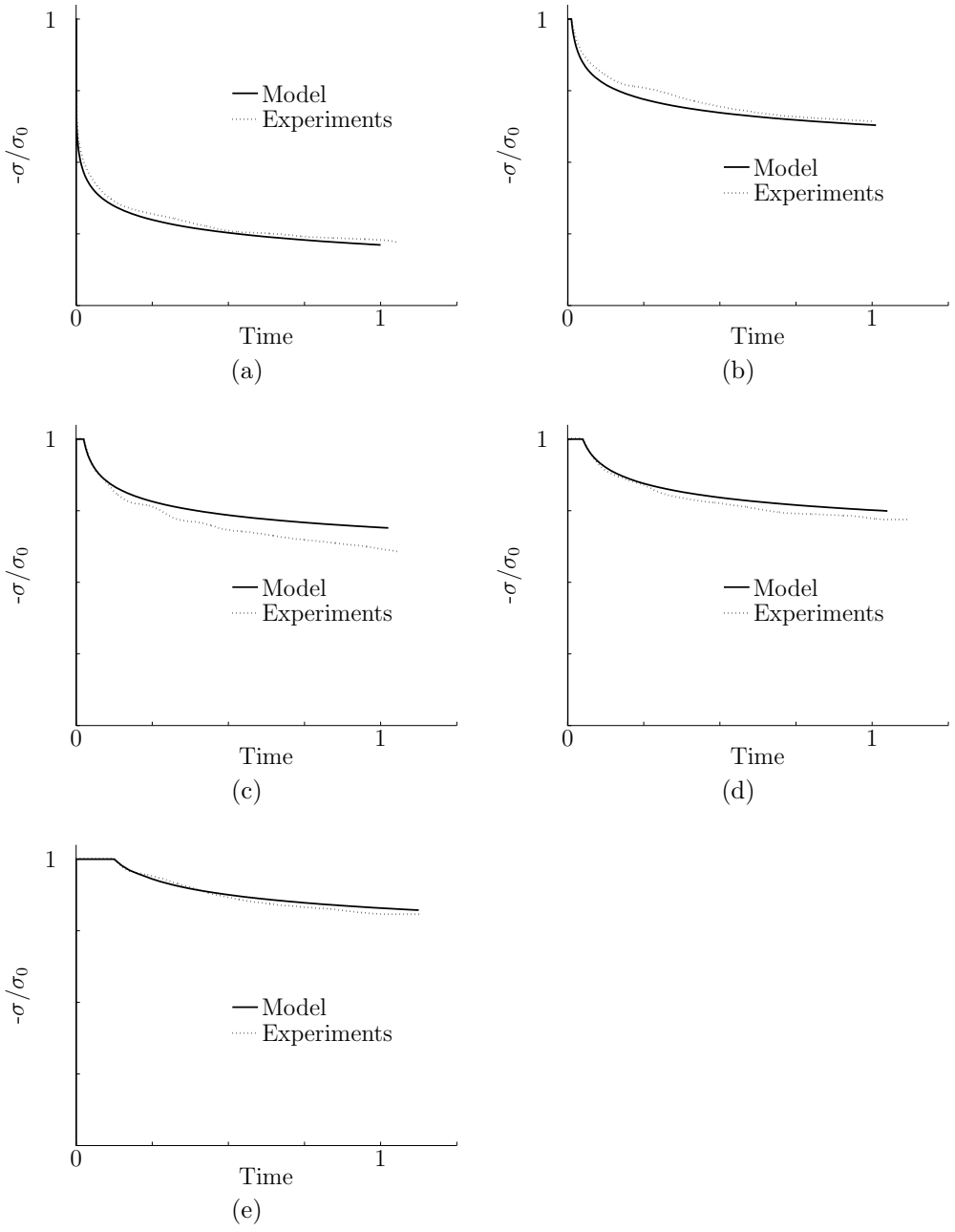

Figure 3.7: Results from the 1-dimensional model compared to experimental data during a relaxation test with a duration of t_0 with the initial pressure. The pressure were held constant before locking the deformation for: (a) t_1, (b) t_2, (c) t_3, (d) t_4 and (e) t_5. Notice that the stress axis has been normalized using the normalization stress σ_0. The time axis is also normalized.

4 Generalized 3D model - isotropic creep

The one dimensional constitutive model presented in equations (3.3) were generalized to three dimensions and implemented in Matlab as a finite element (FE) code. To do this it was assumed that the creep response of the material is isotropic i.e. all the anisotropy is captured by a pure-elastic orthotropic part. It was also assumed that the creep strains are incompressible, i.e. $\varepsilon_{ii}^{cr} = 0$. These assumptions were made because of the lack of experimental data on the creep response in different material directions. Because of the assumption that the creep strains are incompressible the model is separated into a compressible part (the anisotropic elastic part) and an incompressible part.

4.1 Theory

4.1.1 Isotropic viscous part

The assumptions stated above leads to the following formulation of the stress rate in three dimensions for the viscous part of the model, cf. [2]

$$\dot{\sigma}_{ij} = D_{ijkl}\dot{\varepsilon}^{e}_{kl} = D_{ijkl}\left(\dot{\varepsilon}_{kl} - \dot{\varepsilon}^{cr}_{kl}\right) \tag{4.1}$$

where D_{ijkl} is the isotropic elastic stiffness tensor

$$D_{ijkl} = 2G\left[\frac{1}{2}\left(\delta_{ik}\delta_{jl} + \delta_{il}\delta_{jk}\right) + \frac{\nu}{1-2\nu}\delta_{ij}\delta_{kl}\right] \tag{4.2}$$

and G is the shear modulus defined as

$$G = \frac{E}{2(1+\nu)}$$

In matrix form the elastic stiffness is written as

$$\mathbf{D} = \frac{E}{(1+\nu)(1-2\nu)}\begin{bmatrix} 1-\nu & \nu & \nu & 0 & 0 & 0 \\ \nu & 1-\nu & \nu & 0 & 0 & 0 \\ \nu & \nu & 1-\nu & 0 & 0 & 0 \\ 0 & 0 & 0 & \frac{1-2\nu}{2} & 0 & 0 \\ 0 & 0 & 0 & 0 & \frac{1-2\nu}{2} & 0 \\ 0 & 0 & 0 & 0 & 0 & \frac{1-2\nu}{2} \end{bmatrix} \tag{4.3}$$

The creep strain rate in (4.1) is

$$\dot{\varepsilon}^{cr}_{kl} = \left(\frac{\sigma_{eff}}{\sigma_0}\right)^{m}\frac{3s_{ij}}{2\sigma_{eff}} \tag{4.4}$$

Using von Mises criterion the effective stress σ_{eff} is defined as

$$\sigma_{eff} = \sqrt{\frac{3}{2} s_{ij} s_{ij}} \tag{4.5}$$

where the deviatoric stress tensor s_{ij} is defined as

$$s_{ij} = \sigma_{ij} - \frac{1}{3}\sigma_{kk}\delta_{ij} \tag{4.6}$$

4.1.2 Orthotropic elastic part

The stress rate for the orthotropic pure elastic part is given as

$$\dot{\sigma}_{ij} = D^*_{ijkl}\dot{\varepsilon}_{kl} \tag{4.7}$$

where the anisotropic elastic stiffness tensor, D^*_{ijkl} is

$$D^*_{ijkl} = C^{-1}_{ijkl} \tag{4.8}$$

In matrix form the flexibility tensor, C_{ijkl} is written as

$$\mathbf{C} = \begin{bmatrix} \frac{1}{E_{11}} & -\frac{\nu_{21}}{E_{22}} & -\frac{\nu_{31}}{E_{33}} & 0 & 0 & 0 \\ -\frac{\nu_{12}}{E_{11}} & \frac{1}{E_{22}} & -\frac{\nu_{32}}{E_{33}} & 0 & 0 & 0 \\ -\frac{\nu_{13}}{E_{11}} & -\frac{\nu_{23}}{E_{22}} & \frac{1}{E_{33}} & 0 & 0 & 0 \\ 0 & 0 & 0 & \frac{1}{G_{12}} & 0 & 0 \\ 0 & 0 & 0 & 0 & \frac{1}{G_{13}} & 0 \\ 0 & 0 & 0 & 0 & 0 & \frac{1}{G_{23}} \end{bmatrix} \tag{4.9}$$

It will be assumed that the flexibility tensor C_{ijkl} is symmetric. This gives the following relations

$$\frac{\nu_{12}}{E_{11}} = \frac{\nu_{21}}{E_{22}}; \quad \frac{\nu_{13}}{E_{11}} = \frac{\nu_{31}}{E_{22}}; \quad \frac{\nu_{23}}{E_{22}} = \frac{\nu_{32}}{E_{33}} \tag{4.10}$$

Due to lack of experiments in shear the shear modules G_{12}, G_{13} and G_{23} are assumed to be determined as follows (for orthotropic materials the shear modules are independent parameter)

$$G_{12} = \frac{E_{11}}{2\left(1+\nu_{12}\right)}; \quad G_{13} = \frac{E_{22}}{2\left(1+\nu_{13}\right)}; \quad G_{23} = \frac{E_{33}}{2\left(1+\nu_{23}\right)} \tag{4.11}$$

4.1.3 FE-formulation

As mentioned before the generalization was implemented in a FE-code in Matlab. The FE-code essential solves the nonlinear equilibrium equation. This is done using a Newton-Raphson algorithm whose greatest advantage is that quadratic convergence can be obtained sufficiently close to the solution. In order to obtain quadratic convergence of the Newton-Raphson algorithm, when using a numerical integration algorithm, the tangent stiffness used must be derived from the algorithm. This tangent stiffness is called the *algorithmic tangent stiffness* (ATS). The idea of the Newton-Raphson algorithm is to linearise the nonlinear function in the neighbourhood of a given point using a Taylor series expansion ignoring higher terms, cf. [2]. In this case the nonlinear function is the equilibrium equation

$$\boldsymbol{R}(\boldsymbol{a}) = \boldsymbol{f}_{int} - \boldsymbol{f}_{ext} = \int_V \boldsymbol{B}^{\boldsymbol{T}} \boldsymbol{\sigma} dV - \boldsymbol{f}_{ext} = \boldsymbol{0} \tag{4.12}$$

where $\boldsymbol{f}_{int}$ are the internal forces, $\boldsymbol{f}_{ext}$ are the known and fixed external forces. The stress $\boldsymbol{\sigma}$ is dependent of the nodal displacement $\boldsymbol{a}$. The index notation is temporarily abandoned in favour of the more compact matrix notation. $\boldsymbol{B}$ is the gradient of the shape functions $\boldsymbol{N}$, cf. [5]

$$\boldsymbol{B} = \nabla \boldsymbol{N} = \begin{bmatrix} \dfrac{\partial N_1}{\partial x} & \dfrac{\partial N_2}{\partial x} & \cdots & \dfrac{\partial N_n}{\partial x} \\ \dfrac{\partial N_1}{\partial y} & \dfrac{\partial N_2}{\partial y} & \cdots & \dfrac{\partial N_n}{\partial y} \\ \dfrac{\partial N_1}{\partial z} & \dfrac{\partial N_2}{\partial z} & \cdots & \dfrac{\partial N_n}{\partial z} \end{bmatrix} \tag{4.13}$$

A Taylor expansion of $\boldsymbol{R}$ in the neighbourhood of $\boldsymbol{a}^i$, ignoring higher-order terms, yields

$$\boldsymbol{R}(\boldsymbol{a}^{i+1}) = \boldsymbol{R}(\boldsymbol{a}^i) + \left.\frac{\partial \boldsymbol{R}}{\partial \boldsymbol{a}}\right|_{\boldsymbol{a}^i} \left(\boldsymbol{a}^{i+1} - \boldsymbol{a}^i\right) = \boldsymbol{R}(\boldsymbol{a}^i) + \left.\frac{\partial \boldsymbol{R}}{\partial \boldsymbol{a}}\right|_{\boldsymbol{a}^i} d\boldsymbol{a} \tag{4.14}$$

The derivative in the expression above is calculated using (4.12), where $\boldsymbol{f}_{ext}$ is held fixed

$$\left.\frac{\partial \boldsymbol{R}}{\partial \boldsymbol{a}}\right|_{\boldsymbol{a}^i} = \int_V \boldsymbol{B}^{\boldsymbol{T}} \left.\frac{d\boldsymbol{\sigma}}{d\boldsymbol{a}}\right|_{\boldsymbol{a}^i} dV \tag{4.15}$$

The incremental stress, $d\boldsymbol{\sigma}$, can be expressed in the incremental nodal displacement using the tangential material stiffness $\boldsymbol{D}_t$

$$d\boldsymbol{\sigma}^i = \boldsymbol{D}_t^i d\boldsymbol{\varepsilon}^i = \boldsymbol{D}_t^i \boldsymbol{B} d\boldsymbol{a}^i \tag{4.16}$$

Using this the derivative $d\boldsymbol{\sigma}/d\boldsymbol{a}$ at the point $\boldsymbol{a}_i$ can be written as

$$\left.\frac{d\boldsymbol{\sigma}}{d\boldsymbol{a}}\right|_{\boldsymbol{a}^i} = \boldsymbol{D}_t^i \boldsymbol{B} \tag{4.17}$$

This is used together with (4.15) to define the *tangential stiffness matrix* $\boldsymbol{K}_t^i$

$$\boldsymbol{K}_t^i = \left.\frac{\partial \boldsymbol{R}}{\partial \boldsymbol{a}}\right|_{\boldsymbol{a}^i} = \int_V \boldsymbol{B}^{\boldsymbol{T}} \boldsymbol{D}_t^i \boldsymbol{B} dV \tag{4.18}$$

where the tangential material stiffness $\boldsymbol{D}_t^i$ is the ATS defined as

$$\boldsymbol{D}_{ATS}^i = \boldsymbol{D}_t^i = \left.\frac{d\boldsymbol{\sigma}}{d\boldsymbol{\varepsilon}}\right|_{\boldsymbol{a}^i} \tag{4.19}$$

In index notation $\boldsymbol{D}_{ATS}^i$ is written as

$$D_{ijkl}^{ATS} = \frac{d\sigma_{ij}^{(2)}}{d\varepsilon_{kl}^{(2)}} \tag{4.20}$$

4.2 Numerical integration

In this section the numerical integration used to calculate the new stress state and the ATS tensor is described.

4.2.1 Stress state

The stress in one of the isotropic viscous "legs" in the updated state is written as

$$\sigma_{ij}^{(2)} = D_{ijkl}\left(\varepsilon_{kl}^{(2)} - \varepsilon_{kl}^{cr(2)}\right) \tag{4.21}$$

where the superscript (2) is referring to stress in the current state. The creep strain $\varepsilon_{kl}^{cr(2)}$ are calculated by numerical integration of (4.4) using the backward Euler method. The backward Euler method is a fully implicit integration scheme that evaluates the integral in the current state, which is unknown. This leads to the need for a iteratively solution scheme which demands a larger computational effort than a fully explicit scheme which uses only known quantities to solve the new state. The advantage with the backward Euler method is that it is unconditional stable and more accurate than a explicit scheme. Integrating (4.4) using backward Euler the updated creep strain becomes

$$\varepsilon_{kl}^{cr(2)} = \varepsilon_{kl}^{cr(1)} + \int_1^2 \dot{\varepsilon}_{kl}^{cr} dt \approx \varepsilon_{kl}^{cr(1)} + \left(\frac{\sigma_{eff}^{(2)}}{\sigma_0}\right)^m \frac{3}{2}\frac{s_{kl}^{(2)}}{\sigma_{eff}^{(2)}}\Delta t \tag{4.22}$$

where the notation $\varepsilon_{kl}^{cr(1)}$ is referring to the creep strain in the last state of equilibrium as state 1. By inserting this into (4.21) the following expression of the stress in the current state is obtained

$$\sigma_{ij}^{(2)} = D_{ijkl}\left[\varepsilon_{kl}^{(2)} - \varepsilon_{kl}^{cr(1)} - \left(\frac{\sigma_{eff}^{(2)}}{\sigma_0}\right)^m \frac{3}{2}\frac{s_{kl}^{(2)}}{\sigma_{eff}^{(2)}}\Delta t\right] \tag{4.23}$$

The isotropic elastic stiffness tensor D_{ijkl} given by (4.2) couples the deviatoric stress s_{ij} to the deviatoric strain e_{ij} as

$$s_{ij} = D_{ijkl}e_{kl}^e = 2G\left[\frac{1}{2}\left(\delta_{ik}\delta_{jl} + \delta_{il}\delta_{jk}\right)e_{kl}^e + \frac{\nu}{1-2\nu}\delta_{ij}\delta_{kl}e_{kl}^e\right] = 2Ge_{ij}^e \tag{4.24}$$

This is used to rewrite equation (4.23) as

$$s_{ij}^{(2)} = 2G\left[e_{ij}^{(2)} - e_{ij}^{cr(1)} - \left(\frac{\sigma_{eff}^{(2)}}{\sigma_0}\right)^m \frac{3}{2}\frac{s_{ij}^{(2)}}{\sigma_{eff}^{(2)}}\Delta t\right] \tag{4.25}$$

where it has been used that the creep strain are assumed to be incompressible, i.e.

$$\varepsilon_{kk}^{cr} = 0 \quad \Rightarrow \quad \varepsilon_{ij}^{cr} = e_{ij}^{cr} \tag{4.26}$$

Equation (4.25) is rewritten once more to obtain the following expression for the deviatoric stress in the current state

$$s_{ij}^{(2)} = \frac{2G\Delta e_{ij}}{1 + 3G\left(\frac{\sigma_{eff}^{(2)}}{\sigma_0}\right)^m \frac{1}{\sigma_{eff}^{(2)}}\Delta t} \tag{4.27}$$

where

$$\Delta e_{ij} = e_{ij}^{(2)} - e_{ij}^{cr(1)} \tag{4.28}$$

By multiplying each side of equation (4.25) with itself and $\frac{3}{2}$ and finally taking the square root of each side the following equation is obtained

$$\sqrt{\frac{3}{2}s_{ij}^{(2)}s_{ij}^{(2)}}\left(1 + 3G\left(\frac{\sigma_{eff}^{(2)}}{\sigma_0}\right)^m \frac{\Delta t}{\sigma_{eff}^{(2)}}\right) = 2G\sqrt{\frac{3}{2}\Delta e_{ij}\Delta e_{ij}} \tag{4.29}$$

where one can identify the square root on the far left hand side as the effective stress at state 2 (see equation (4.5)). This gives the following final expression for the effective stress

$$\sigma_{eff}^{(2)} + 3G\left(\frac{\sigma_{eff}^{(2)}}{\sigma_0}\right)^m \Delta t = 2G\sqrt{\frac{3}{2}\Delta e_{ij}\Delta e_{ij}} \tag{4.30}$$

The only unknown in this scalar equation is the effective stress $\sigma_{eff}^{(2)}$ given the new strain $\varepsilon_{ij}^{(2)}$. This equation is solved for $\sigma_{eff}^{(2)}$ using a one-dimensional Newton-Raphson algorithm. Using the resulting effective stress the deviatoric stress in the current state $s_{ij}^{(2)}$ is then calculated using (4.27). Finally the stress in the current state $\sigma_{ij}^{(2)}$ is calculated using the effective and deviatoric stresses in (4.23).

$$\sigma_{ij}^{(2)} = D_{ijkl}\left[\varepsilon_{kl}^{(2)} - \varepsilon_{kl}^{cr(1)} - \left(\frac{\sigma_{eff}^{(2)}}{\sigma_0}\right)^m \frac{3}{2}\frac{s_{kl}^{(2)}}{\sigma_{eff}^{(2)}}\Delta t\right] \tag{4.31}$$

$\sigma_{eff}^{(2)}$ is obtained implicitly from

$$\sigma_{eff}^{(2)} + 3G\left(\frac{\sigma_{eff}^{(2)}}{\sigma_0}\right)^m \Delta t = 2G\sqrt{\frac{3}{2}\Delta e_{ij}\Delta e_{ij}} \tag{4.32}$$

The deviatoric stress in state 2 is

$$s_{ij}^{(2)} = \frac{2G\Delta e_{ij}}{1 + 3G\left(\frac{\sigma_{eff}^{(2)}}{\sigma_0}\right)^m \frac{1}{\sigma_{eff}^{(2)}}\Delta t} \tag{4.33}$$

where

$$\Delta e_{ij} = e_{ij}^{(2)} - e_{ij}^{cr(1)} \tag{4.34}$$

These equations are used to calculate the stress in each of the two viscous "legs" of the model (see figure 3.1). The reformulations above results in the scalar equation (4.32) which has to be solved implicitly. From a computational point of view this is very effective in comparison to solving a coupled system of equations. This reformulation is made possible because of the assumption that the creep strains are isotropic and incompressible.

The stress in the anisotropic elastic leg are obtained by integration of equation (4.7)

$$\sigma_{ij}^{(2)} = D_{ijkl}^{*}\varepsilon_{kl}^{(2)} \tag{4.35}$$

The total stress is the sum of the stresses in the three legs

$$\sigma_{ij}^{tot(2)} = \sigma_{ij}^{\infty(2)} + \sigma_{ij}^{1(2)} + \sigma_{ij}^{2(2)} \tag{4.36}$$

4.2.2 Algorithmic tangent stiffness

According to (4.31) the stress at the current state is

$$\sigma_{ij}^{(2)} = D_{ijkl}\left[\varepsilon_{kl}^{(2)} - \varepsilon_{kl}^{cr(1)} - \left(\frac{\sigma_{eff}^{(2)}}{\sigma_0}\right)^m \frac{3}{2}\frac{s_{kl}^{(2)}}{\sigma_{eff}^{(2)}}\Delta t\right] \tag{4.37}$$

By differentiation of this equation the following is obtained

$$d\sigma_{ij}^{(2)} = D_{ijkl}\left[d\varepsilon_{kl}^{(2)} - \frac{A_c}{G}s_{kl}^{(2)}d\sigma_{eff}^{(2)} - \frac{A_S}{2G}ds_{kl}^{(2)}\right] \tag{4.38}$$

where

$$A_c = \frac{3}{2}G(m-1)\frac{\Delta t}{\sigma_0^m}\left(\sigma_{eff}^{(2)}\right)^{m-2} \tag{4.39}$$

and

$$A_S = 3G\frac{\Delta t}{\sigma_0^m}\left(\sigma_{eff}^{(2)}\right)^{m-1} \tag{4.40}$$

In the same fashion as in (4.24) the isotropic elastic stiffness tensor (4.2) is used to rewrite the following

$$D_{ijkl}s_{kl}^{(2)} = 2Gs_{ij}^{(2)}; \quad D_{ijkl}ds_{kl}^{(2)} = 2Gds_{ij}^{(2)} \tag{4.41}$$

These two expressions are used to rewrite (4.38) as

$$d\sigma_{ij}^{(2)} + A_S ds_{ij}^{(2)} = D_{ijkl}d\varepsilon_{kl}^{(2)} - 2A_c s_{ij}^{(2)}d\sigma_{eff}^{(2)} \tag{4.42}$$

The assumption that the creep strains are incompressible leads to that the differentiated deviatoric stress can be written as

$$ds_{ij}^{(2)} = d\sigma_{ij}^{(2)} - \frac{1}{3}d\sigma_{kk}^{(2)}\delta_{ij} = d\sigma_{ij}^{(2)} - Kd\varepsilon_{kk}^{(2)}\delta_{ij} = d\sigma_{ij}^{(2)} - Kd\varepsilon_{kl}^{(2)}\delta_{ij}\delta_{kl} \tag{4.43}$$

where K is the bulk modulus defined as

$$K = \frac{E}{3(1-2\nu)} \tag{4.44}$$

Insertion of (4.43) leads to that equation (4.42) can be written as

$$d\sigma_{ij}^{(2)} = \frac{1}{1+A_S}\left[D_{ijkl}d\varepsilon_{kl}^{(2)} - 2A_c s_{ij}^{(2)}d\sigma_{eff}^{(2)} + A_S K d\varepsilon_{kl}^{(2)}\delta_{ij}\delta_{kl}\right] \tag{4.45}$$

In accordance with (4.32) the effective stress at the current state can be written as

$$\sigma_{eff}^{(2)} + 3G\left(\frac{\sigma_{eff}^{(2)}}{\sigma_0}\right)^m \Delta t = 2G\sqrt{\frac{3}{2}\Delta e_{ij}\Delta e_{ij}} \tag{4.46}$$

where

$$\Delta e_{ij} = e_{ij}^{(2)} - e_{ij}^{cr(1)} \tag{4.47}$$

Differentiation of the effective stress gives

$$d\sigma_{eff}^{(2)} + 3Gm\frac{\left(\sigma_{eff}^{(2)}\right)^{(m-1)}}{\sigma_0^m}\Delta t d\sigma_{eff}^{(2)} = G\sqrt{\frac{6}{\Delta e_{mn}\Delta e_{mn}}}\Delta e_{ij} de_{ij}^{(2)} \tag{4.48}$$

Using the definition of the deviatoric strain $\Delta e_{ij} de_{ij}^{(2)}$ can be rewritten as

$$\Delta e_{ij} de_{ij}^{(2)} = \Delta e_{ij} d\varepsilon_{ij}^{(2)} - \frac{1}{3} d\varepsilon_{kk}^{(2)} \Delta e_{ij}\delta_{ij} = \Delta e_{ij} d\varepsilon_{ij}^{(2)} \tag{4.49}$$

This leads to that equation (4.48) can be rewritten as

$$d\sigma_{eff}^{(2)} = A_{eff}\Delta e_{ij} d\varepsilon_{ij}^{(2)} \tag{4.50}$$

where

$$A_{eff} = \frac{G\sqrt{\dfrac{6}{\Delta e_{mn}\Delta e_{mn}}}}{1 + mA_S} \tag{4.51}$$

where A_S is given by (4.40). By inserting equation (4.50) into equation (4.45) the final expression for the ATS is obtained

$$D_{ijkl}^{ATS} = \frac{d\sigma_{ij}^{(2)}}{d\varepsilon_{kl}^{(2)}} = \frac{1}{1+A_S}\left[D_{ijkl} - 2A_{eff}A_c s_{ij}^{(2)}\Delta e_{kl} + KA_S\delta_{ij}\delta_{kl}\right] \quad (4.52)$$

where Δe_{kl} *is*

$$\Delta e_{kl} = e_{kl}^{(2)} - e_{kl}^{cr(1)}$$

A_S *is*

$$A_S = 3G\frac{\Delta t}{\sigma_0^m}\left(\sigma_{eff}^{(2)}\right)^{m-1}$$

A_c *is*

$$A_c = \frac{3}{2}G(m-1)\frac{\Delta t}{\sigma_0^m}\left(\sigma_{eff}^{(2)}\right)^{m-2}$$

and A_{eff} *is*

$$A_{eff} = \frac{G\sqrt{\dfrac{6}{\Delta e_{mn}\Delta e_{mn}}}}{1+mA_S}$$

This expression for the tangent stiffness is used for the two viscous legs of the model. The total tangent stiffness is calculated as the sum of stiffnesses of the three legs of the model

$$D_{ijkl}^{totATS} = D_{ijkl}^{*} + D_{ijkl}^{1ATS} + D_{ijkl}^{2ATS} \quad (4.53)$$

4.3 Implementation

A finite element program using the generalized three dimensional constitutive model were implemented in Matlab. The equations to calculate the algorithmic tangent stiffness (4.52) and the stress state (4.31) were implemented in two separate functions. The Newton-Raphson algorithm used to solve the non-linear equations are shown in box 4.1

Box 4.1 Newton-Raphson algorithm

- Initiation of quantities

$$\boldsymbol{a}_0 = \mathbf{0}; \quad \boldsymbol{\sigma}_0 = \mathbf{0}; \quad \boldsymbol{\varepsilon}_0 = \mathbf{0}; \quad \boldsymbol{f}_{ext,0} = \mathbf{0}; \quad \boldsymbol{f}_{int,0} = \mathbf{0};$$

- For time/load step $n = 0, 1, 2, 3, ..., N_{max}$
  - Determine new external load $f_{ext} = f_{n+1}$
  - Initiation of iteration quantities

$$\boldsymbol{a}^0 = \boldsymbol{a}_n$$

  - Iterate $i = 1, 2, ...$ until $|\boldsymbol{R}| = |\boldsymbol{f}_{int} - \boldsymbol{f}_{ext}| < tolerance$
    - Calculate $\boldsymbol{D}_{ATS}^{i-1}$
    - Calculate $\boldsymbol{K}_t^i = \int_V \boldsymbol{B}^{\boldsymbol{T}} \boldsymbol{D}_{ATS}^{i-1} \boldsymbol{B} dV$
    - Calculate $\boldsymbol{a}^i$ from $\boldsymbol{K}_t^i (\boldsymbol{a}^i - \boldsymbol{a}^{i-1}) = \boldsymbol{f}_{ext} - \boldsymbol{f}_{int}$
    - Calculate $\boldsymbol{\varepsilon}^i = \boldsymbol{B}\boldsymbol{a}^i$
    - Calculate $\boldsymbol{\sigma}^{\boldsymbol{i}}$
    - Calculate $\boldsymbol{f}_{int} = \int_V \boldsymbol{B}^{\boldsymbol{T}} \boldsymbol{\sigma}^i dV$
  - End iteration loop
  - Accept the new quantities

$$\boldsymbol{a}_{n+1} = \boldsymbol{a}^i; \quad \boldsymbol{\sigma}_{n+1} = \boldsymbol{\sigma}^i; \quad \boldsymbol{\varepsilon}_{n+1} = \boldsymbol{\varepsilon}^i; \quad \boldsymbol{f}_{int}$$

- End load step loop

4.4 Parameters

The generalized three dimensional constitutive model contains thirteen parameters in addition to seven from the one dimensional model. Theses parameters are: Poisson's ratios ν for the isotropic part, the Young's modules, the shear modules and Poisson's ratios for the anisotropic part of the model. Due to the symmetry of the anisotropic stiffness tensor (4.9) the number of new parameters are reduced to ten independent parameters using (4.10). The independent parameters are presented in table 4.1.

Table 4.1: Model parameters

E_{11}	Elastic orthotropic part
E_{22}	
E_{33}	
ν_{12}	
ν_{13}	
ν_{23}	
G_{12}	
G_{13}	
G_{23}	
E_1	Non-linear creep leg 1
ν_1	
m_1	
σ_{0_1}	
E_2	Non-linear creep leg 2
ν_2	
m_2	
σ_{0_2}	

As in the one dimensional case the parameters were determined by curve fitting the model to the experimental data. The same experimental data were used as in the one dimensional case with the addition of the strain controlled uniaxial tensile tests to fit the anisotropic parameters. The uniaxial experiments are further described in section 2.5.3. Because the model is separated into a compressible and an incompressible part the uniaxial response is dependent on the isotropic Poisson's ratio. To solve this the isotropic Poisson's ratio were fixed at $\nu_1 = \nu_2 = constant$ before the parameter identification. Because of the total lack of experimental data to determine Poisson's ratio this choice were a pure guess.

4.5 Results

All the results presented in this section are produced using the same model and the same set of parameters. The figures are showing the results from the model compared with experimental data.

4.5.1 Uniaxial tests

Figure 4.1 is showing the stress-strain curves in the three material directions from the model compared with experimental data during loading and unloading. The uniaxial tensile experiments in the machine- and the cross machine direction are presented in section 2.5.3. The compression experiment in the thickness direction are presented in section 2.6. As the figure shows the model captures the initial stiffness very well in all three directions but not the viscous effects. These curves were used to determine the model parameters in table 4.1 coupled to the initial stiffness.

4.5.2 Repeated compression

Figure 4.2 is showing the results from the model with repeated compression and rest with the duration t_9 between the compression cycles. The fourth cycle (cycle d) was carried out after a recovery period of t_{10}. Figure 4.3 is showing the results from the model with repeated compression with a recovery period with the duration t_7 between the cycles. The experiments are further explained in section 2.7.2. All of these curves were used when the model parameters in table 4.1 were determined.

4.5.3 Constant pressure before relaxation test

Figure 4.4a is showing the result from the model compared to experimental data during a t_0 relaxation test where an initial pressure is applied and the height is locked after a t_1 relaxation period. This curve were used in the curve fitting procedure to determine the model parameters in table 4.1. The figures 4.4b to 4.4e is showing a comparison between the result from the model and experimental data during t_0 relaxation tests where the initial pressure were hold constant for t_2, t_2, t_4 and t_5 respectively before the height were fixed. These curves were not used when the model parameters in table 4.1 were determined. The experiments are further described in section 2.7.1.

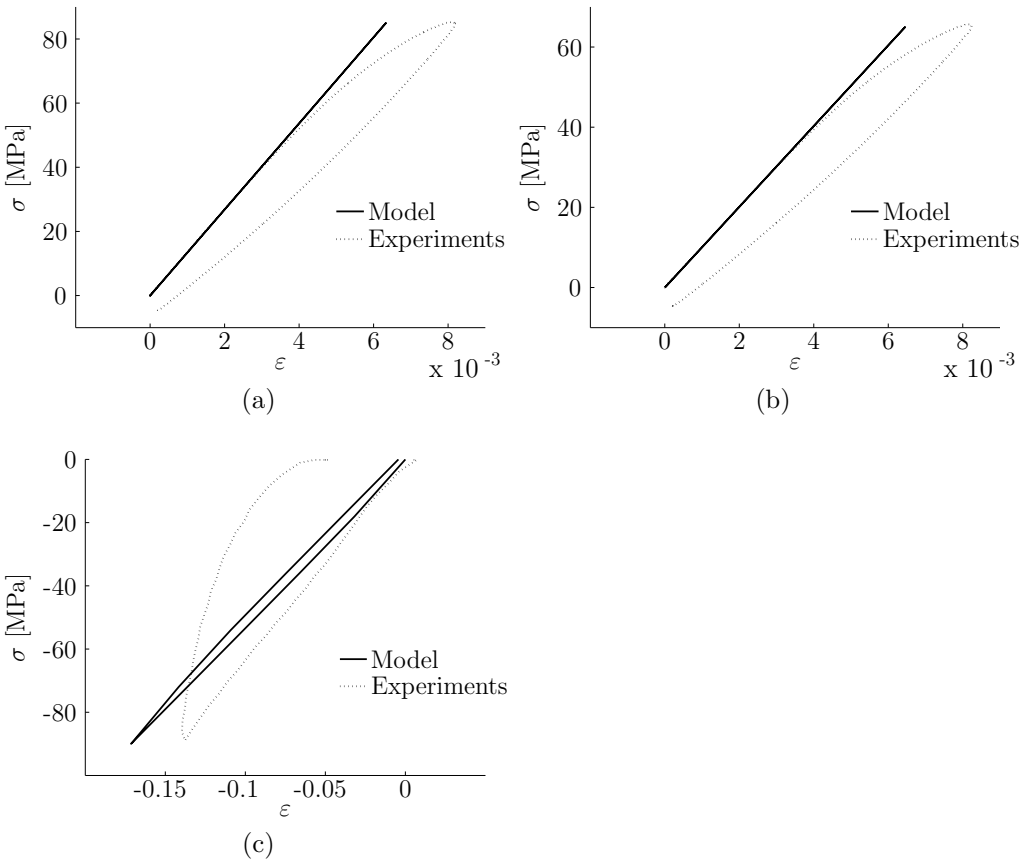

Figure 4.1: The graphs are showing the results from the model compared with experimental data for the stress-strain curves in the three material directions during loading and unloading: (a) machine direction, (b) cross machine direction and (c) thickness direction. These curves were used when determining the model parameters in table 4.1.

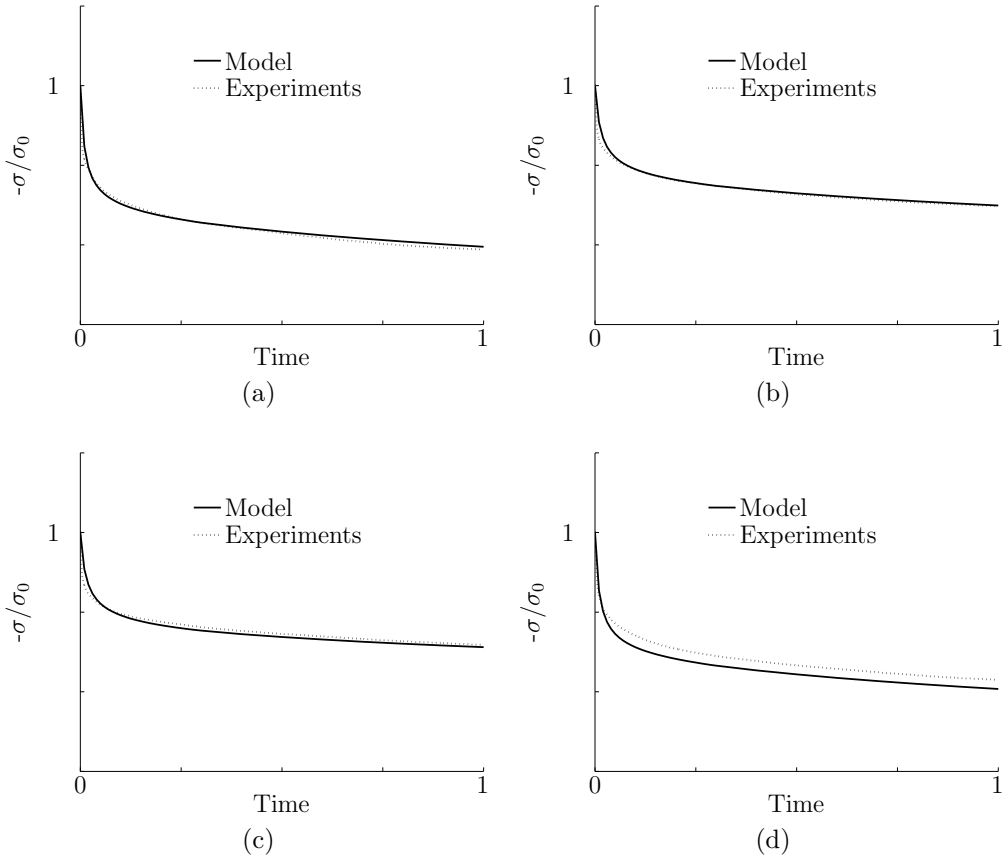

Figure 4.2: The graphs are showing the results from the 3-dimensional model compared with experimental data when the same test piece is exposed to repeated compression and relaxation. Graphs a-c is showing the first three cycles with t_9 rest between the cycles. Cycle (d) was carried out after t_{10} recovery. These four curves were used when the model parameters in table 4.1 were determined. Notice that the stress axis has been normalized using the normalization stress σ_0. The time axis is also normalized.

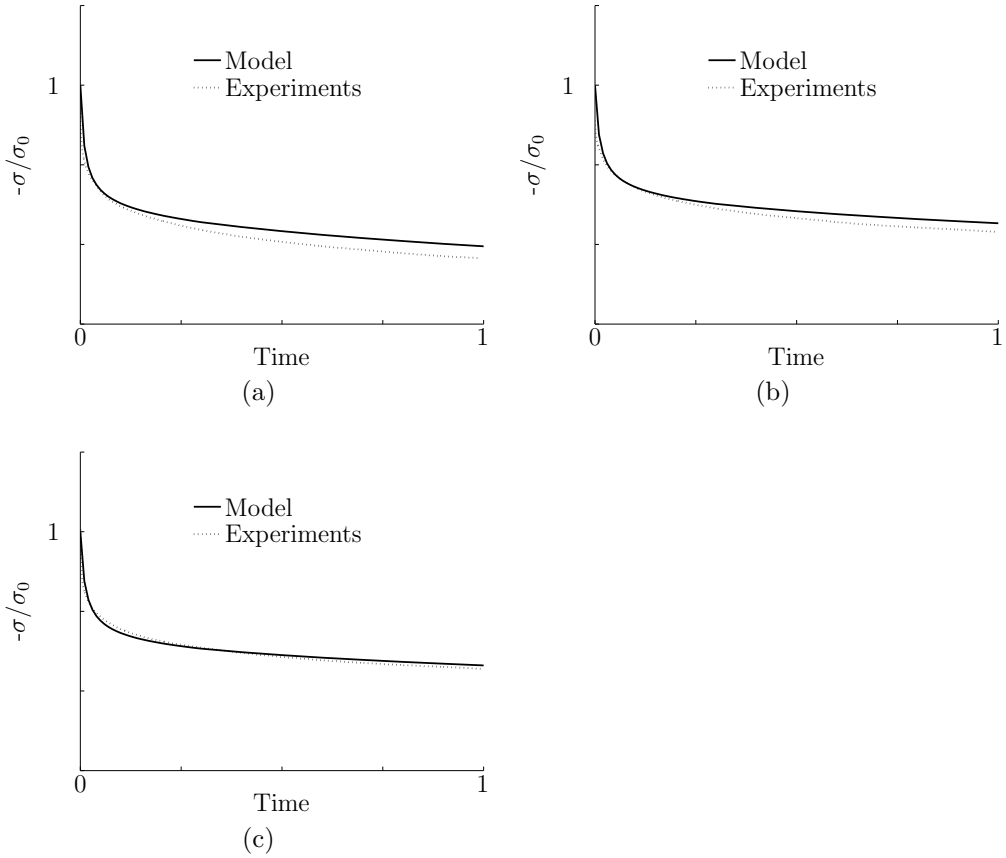

Figure 4.3: The graphs are showing the results from the 3-dimensional model compared with experimental data when the same test piece is exposed to repeated compression and relaxation. The test piece has recovered for t_6 between the cycles. These curves were used when the model parameters in table 4.1 were determined. Notice that the stress axis has been normalized using the normalization stress σ_0. The time axis is also normalized.

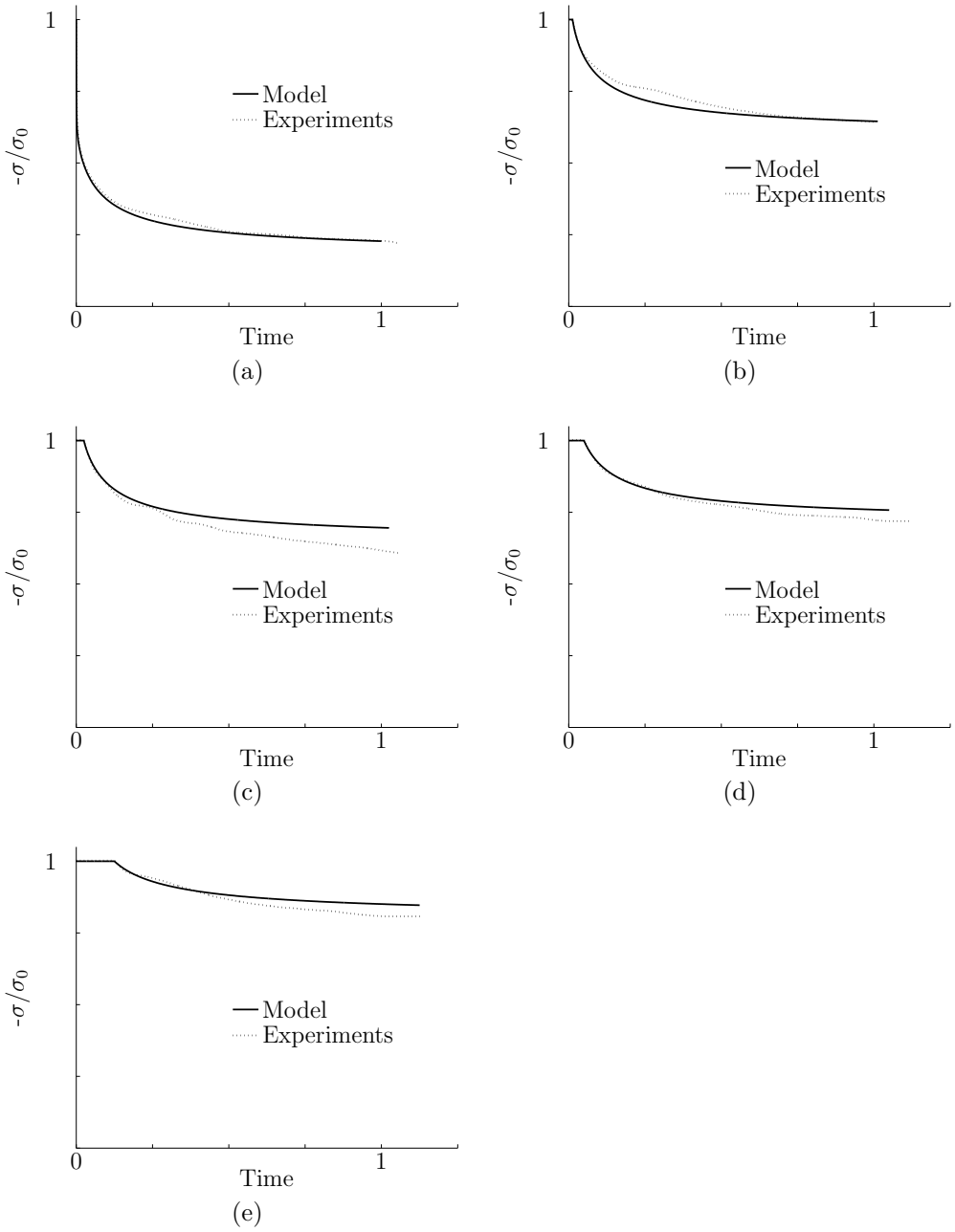

Figure 4.4: The graphs are showing the results from the 3-dimensional model compared to experimental data during a relaxation test with a duration of t_0 with the initial pressure. The pressure were held constant before locking the deformation for: (a) t_1, (b) t_2, (c) t_3, (d) t_4 and (e) t_5. Notice that the stress axis has been normalized using the normalization stress σ_0. The time axis is also normalized.

5 Generalized 3D model - anisotropic creep

The three dimensional model presented in section 4 were further generalized to include anisotropic creep as well as anisotropic elasticity. This was done to be able to better capture the in-plane response from the uniaxial tensile test described in section 2.5.3. To capture the in-plane response it was necessary to extend the model with one additional viscous part.

5.1 Theory

The stress rate for the viscous parts are given by

$$\dot{\sigma}_{ij} = D^*_{ijkl}\dot{\varepsilon}^e_{kl} = D^*_{ijkl}\left(\dot{\varepsilon}_{kl} - \dot{\varepsilon}^{cr}_{kl}\right) \tag{5.1}$$

where the anisotropic elastic stiffness tensor D^*_{ijkl} is

$$D^*_{ijkl} = C^{-1}_{ijkl} \tag{5.2}$$

The flexibility tensor C_{ijkl} is given by (4.9). The creep strain $\dot{\varepsilon}^{cr}_{kl}$ is given by (4.4) as

$$\dot{\varepsilon}^{cr}_{kl} = \left(\frac{\sigma_{eff}}{\sigma_0}\right)^m \frac{3s_{ij}}{2\sigma_{eff}} \tag{5.3}$$

with the effective stress σ_{eff} as (4.5) and the deviatoric stress s_{ij} as (4.6).

5.2 Numerical integration

5.2.1 Stress state

The stress in the updated state can be written as

$$\sigma^{(2)}_{ij} = D^*_{ijkl}\left(\varepsilon^{(2)}_{kl} - \varepsilon^{cr(2)}_{kl}\right) \tag{5.4}$$

where the superscript (2) is referring to stress in the current state as state 2. The creep strain $\varepsilon^{cr(2)}_{kl}$ are calculated by numerical integration of (4.4) using the backward Euler method

$$\varepsilon^{cr(2)}_{kl} = \varepsilon^{cr(1)}_{kl} + \int_1^2 \dot{\varepsilon}^{cr}_{kl}dt \approx \varepsilon^{cr(1)}_{kl} + \left(\frac{\sigma^{(2)}_{eff}}{\sigma_0}\right)^m \frac{3}{2}\frac{s^{(2)}_{kl}}{\sigma^{(2)}_{eff}}\Delta t \tag{5.5}$$

This is inserted into (5.4) to obtain the final expression for the stress in the current state.

$$\sigma_{ij}^{(2)} = D_{ijkl}^{*}\left[\varepsilon_{kl}^{(2)} - \varepsilon_{kl}^{cr(1)} - \left(\frac{\sigma_{eff}^{(2)}}{\sigma_0}\right)^{m}\frac{3}{2}\frac{s_{kl}^{(2)}}{\sigma_{eff}^{(2)}}\Delta t\right] \tag{5.6}$$

This expression for the stress can not be reformulated into one scalar equation in the same fashion as for the model with isotropic creep. Instead the whole system of equations has to be solved iteratively which requires much more computational work than just solving a scalar equation. The stress in the pure-elastic part of the model is calculated as

$$\sigma_{ij}^{(2)} = D_{ijkl}^{*}\varepsilon_{kl}^{(2)} \tag{5.7}$$

The total stress is the sum of the stresses in the four parts

$$\sigma_{ij}^{tot(2)} = \sigma_{ij}^{\infty(2)} + \sigma_{ij}^{1(2)} + \sigma_{ij}^{2(2)} + \sigma_{ij}^{3(2)} \tag{5.8}$$

5.2.2 Algorithmic tangent stiffness

The algorithmic tangent stiffness tensor is derived in a different manner than for the isotropic creep. The ATS tensor is derived using a residual function which is exactly zero for every strain. This derivation scheme has been used for plasticity but is here adopted to viscoelasticity, cf. [6]. An alternative method of solving the nonlinear equations is the *Newton-Schur approach* which has the advantage of needing less computational work, cf. [7].

The stress in the current state (5.4) is differentiated in order to obtain an expression for the ATS tensor

$$d\sigma_{ij}^{(2)} = D_{ijmn}^{*}\left(d\varepsilon_{mn}^{(2)} - d\varepsilon_{mn}^{cr(2)}\right) = D_{ijmn}^{*}\left(I_{mnkl} - \frac{d\varepsilon_{mn}^{cr(2)}}{d\varepsilon_{kl}^{(2)}}\right)d\varepsilon_{kl}^{(2)} \tag{5.9}$$

where I_{klmn} is a symmetric fourth order unity tensor defined as

$$I_{ijkl} = \frac{1}{2}\left(\delta_{ik}\delta_{jl} + \delta_{il}\delta_{jk}\right) \tag{5.10}$$

The ATS tensor is obtained by using (5.9) together with the definition of the ATS tensor (4.53)

$$D_{ijkl}^{ATS} = \frac{d\sigma_{ij}^{(2)}}{d\varepsilon_{kl}^{(2)}} = D_{ijmn}^{*}\left(I_{mnkl} - \frac{d\varepsilon_{mn}^{cr(2)}}{d\varepsilon_{kl}^{(2)}}\right) \tag{5.11}$$

The residual function is obtained using (5.4) as

$$R_{ij}\left(\varepsilon_{kl},\varepsilon_{kl}^{cr}\right)=\sigma_{ij}^{(2)}-D_{ijkl}^{*}\left(\varepsilon_{kl}^{(2)}-\varepsilon_{kl}^{cr(2)}\right)=0\quad\forall\varepsilon_{kl}^{(2)} \tag{5.12}$$

This equation should hold for every strain $\varepsilon_{kl}^{(2)}$ which means that the derivative of R_{ij} should be equal to zero for every strain, i.e.

$$\frac{\partial R_{ij}}{\partial\varepsilon_{mn}^{cr(2)}}\frac{d\varepsilon_{mn}^{cr(2)}}{d\varepsilon_{kl}^{(2)}}+\frac{\partial R_{ij}}{\partial\varepsilon_{kl}^{(2)}}=0 \tag{5.13}$$

This is rewritten to obtain the derivative on the far right side in (5.11)

$$\frac{d\varepsilon_{mn}^{cr(2)}}{d\varepsilon_{kl}^{(2)}}=-\left(\frac{\partial R_{ij}}{\partial\varepsilon_{mn}^{cr(2)}}\right)^{-1}\frac{\partial R_{ij}}{\partial\varepsilon_{kl}^{(2)}} \tag{5.14}$$

where

$$\begin{aligned}\frac{\partial R_{ij}}{\partial\varepsilon_{mn}^{cr(2)}} &= -D_{ijmn}^{*}-D_{ijxy}^{*}\left[A^{\varepsilon}\left(D_{xymn}^{*}-\frac{1}{3}D_{aamn}^{*}\delta_{xy}\right)\right.\\ &\quad\left.+B^{\varepsilon}s_{xy}^{(2)}s_{op}^{(2)}D_{opmn}^{*}\right]\end{aligned} \tag{5.15}$$

and

$$\begin{aligned}\frac{\partial R_{ij}}{\partial\varepsilon_{kl}^{(2)}} &= D_{ijkl}^{*}-D_{ijxy}^{*}\left[I_{xykl}-A^{\varepsilon}\left(D_{xykl}^{*}-\frac{1}{3}D_{aakl}^{*}\delta_{xy}\right)\right.\\ &\quad\left.-B^{\varepsilon}s_{xy}^{(2)}s_{op}^{(2)}D_{opkl}^{*}\right]\end{aligned} \tag{5.16}$$

In the two expressions above A^{ε} and B^{ε} are

$$A^{\varepsilon}=\frac{3}{2}\Delta t\frac{\left(\sigma_{eff}^{(2)}\right)^{m-1}}{\sigma_{0}^{m}} \tag{5.17}$$

and

$$B^{\varepsilon}=\frac{9}{4}\left(m-1\right)\Delta t\frac{\left(\sigma_{eff}^{(2)}\right)^{m-3}}{\sigma_{0}} \tag{5.18}$$

As for the model with isotropic creep this is used to calculate the tangent stiffness for the viscous parts of the model. The total tangent stiffness is calculated as the sum of the stiffnesses of the four parts of the model

$$D_{ijkl}^{totATS}=D_{ijkl}^{*}+D_{ijkl}^{1ATS}+D_{ijkl}^{2ATS}+D_{ijkl}^{3ATS} \tag{5.19}$$

5.3 Implementation and paramters

The constitutive model were implemented in a FE-code using Matlab in the same way as the model with isotropic creep, described in section 4.3. Due to the expansion of the model the number of model parameters increases to a total of 42 independent parameters. These are presented in table 5.1. Note that the shear modules has been calculated according to (4.11). The model parameters were determined in the same fashion as for the model with isotropic creep which is described in section 4.4.

Table 5.1: Model parameters

E_{11}^{∞}		E_{11}^{2}	
E_{22}^{∞}		E_{22}^{2}	
E_{33}^{∞}		E_{33}^{2}	
ν_{12}^{∞}		ν_{12}^{2}	
ν_{13}^{∞}		ν_{13}^{2}	
ν_{23}^{∞}	Elastic part	ν_{23}^{2}	Viscoelastic part 2
G_{12}^{∞}		G_{12}^{2}	
G_{13}^{∞}		G_{13}^{2}	
G_{23}^{∞}		G_{23}^{2}	
		m^{2}	
		σ_{0}^{2}	
E_{11}^{1}		E_{11}^{3}	
E_{22}^{1}		E_{22}^{3}	
E_{33}^{1}		E_{33}^{3}	
ν_{12}^{1}		ν_{12}^{3}	
ν_{13}^{1}		ν_{13}^{3}	
ν_{23}^{1}	Viscoelastic part 1	ν_{23}^{3}	Viscoelastic part 3
G_{12}^{1}		G_{12}^{3}	
G_{13}^{1}		G_{13}^{3}	
G_{23}^{1}		G_{23}^{3}	
m^{1}		m^{3}	
σ_{0}^{1}		σ_{0}^{3}	

5.4 Results

All the results presented in this section are produced using the same model and the same set of parameters. The figures are showing the results from the model compared with experimental data.

5.4.1 Uniaxial tests

Figure 5.1 is showing the stress-strain curves in the three material directions from the model compared with experimental data during loading and unloading. The uniaxial tensile experiments in the machine- and the cross machine direction are presented in section 2.5.3. The compression experiment in the thickness direction are presented in section 2.6. As the figure shows the model captures the viscous effects better than the model with isotropic creep. Even so the model does not capture the stress-strain behaviour in out-of-plane compression very well. These curves were used to determine the model parameters in table 5.1.

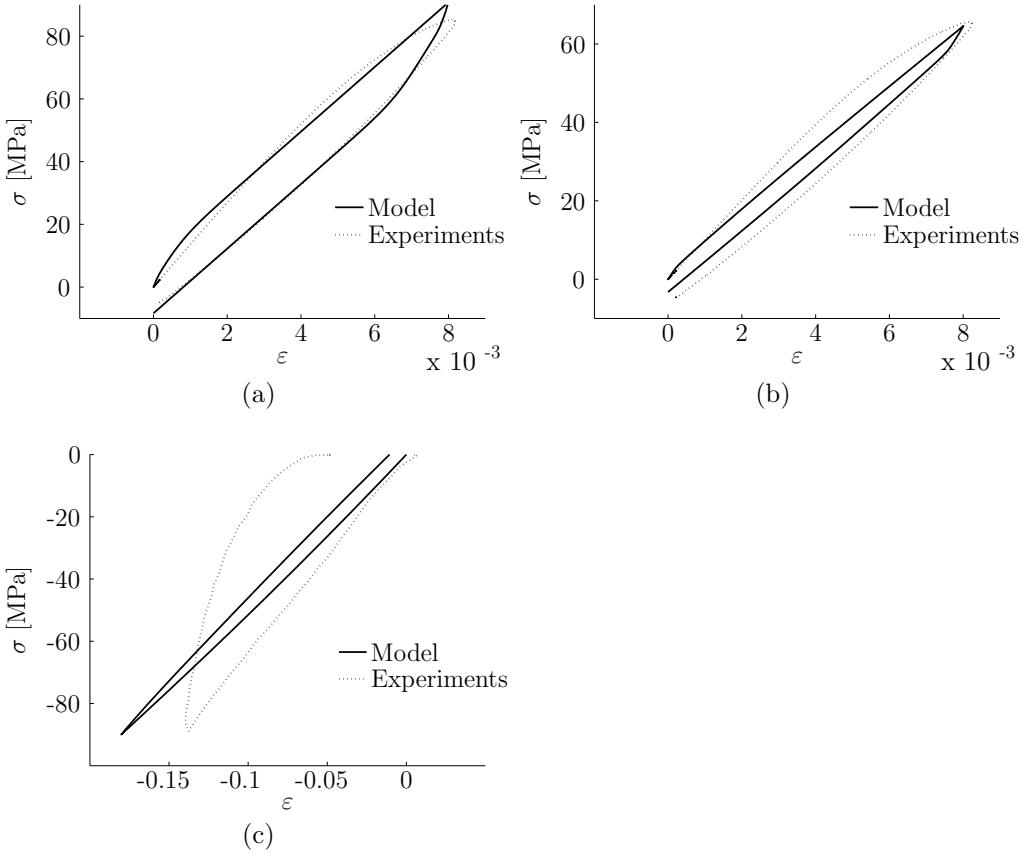

Figure 5.1: The figure is showing the results from the model compared with experimental data for the stress-strain curves in the three material directions during loading and unloading: (a) machine direction, (b) cross machine direction and (c) thickness direction. These curves were used when determining the model parameters in table 5.1.

5.4.2 Repeated compression

Figure 5.2 is showing the results from the model with repeated compression and rest with the duration t_9 between the compression cycles. The fourth cycle (cycle d) was carried out after a recovery period of t_{10}. Figure 5.3 is showing the results from the model with repeated compression with a recovery period with the duration t_7 between the cycles. The experiments are further explained in section 2.7.2. All of these curves were used when the model parameters in table 5.1 were determined.

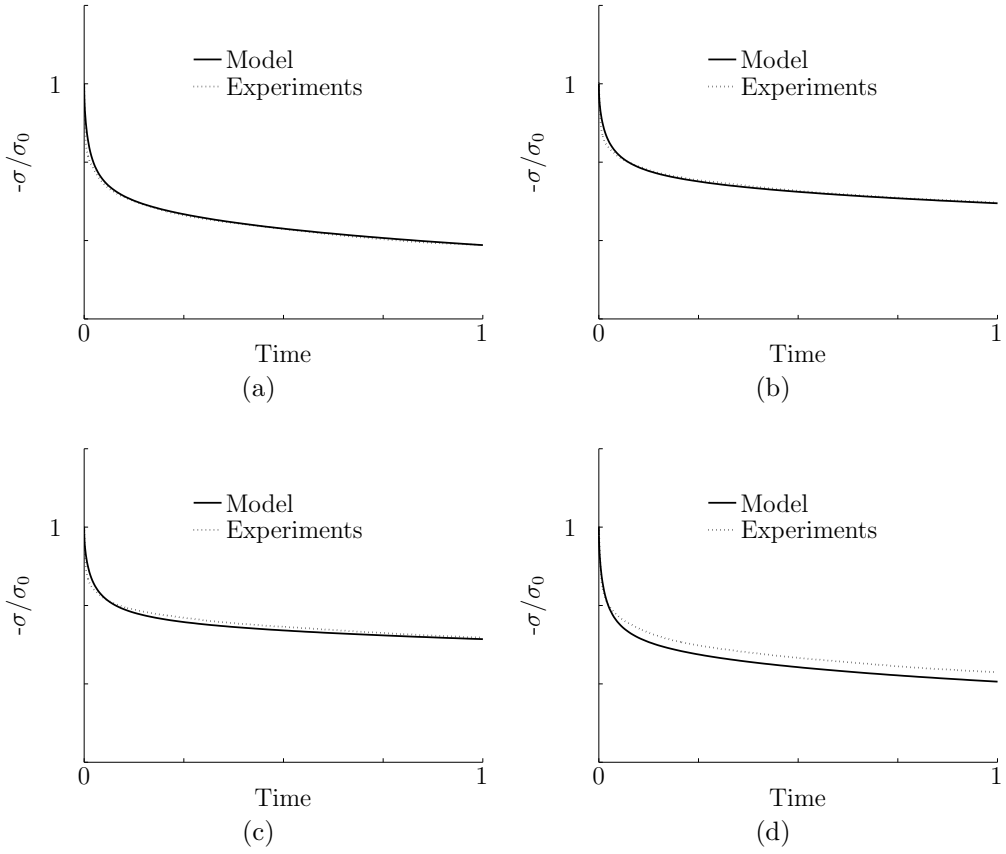

Figure 5.2: The figure is showing the results from the 3-dimensional model compared with experimental data when the same test piece is exposed to repeated compression and relaxation. Graphs a-c is showing the first three cycles with t_9 rest between the cycles. Cycle (d) was carried out after t_{10} recovery. These four curves were used when the model parameters in table 5.1 were determined. Notice that the stress axis has been normalized using the normalization stress σ_0. The time axis is also normalized.

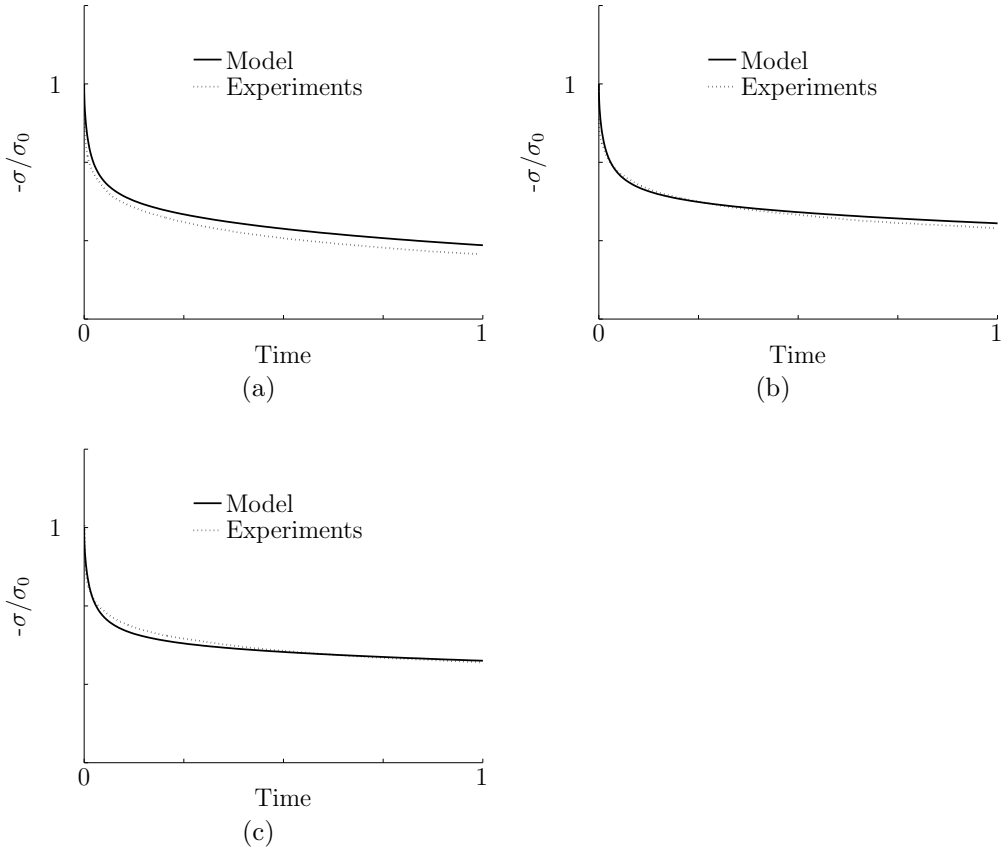

Figure 5.3: The figure is showing the results from the 3-dimensional model compared with experimental data when the same test piece is exposed to repeated compression and relaxation. The test piece has recovered for t_7 between the cycles. These curves were used when the model parameters in table 5.1 were determined. Notice that the stress axis has been normalized using the normalization stress σ_0. The time axis is also normalized.

5.4.3 Constant pressure before relaxation test

Figure 5.4a is showing the result from the model compared to experimental data during a t_0 relaxation test where an initial pressure is applied and the height is locked after a t_1 relaxation period. This curve were used in the curve fitting procedure to determine the model parameters in table 5.1. The figures 5.4b to 5.4e is showing a comparison between the result from the model and experimental data during t_0 relaxation tests where the initial pressure were hold constant for t_2, t_2, t_4 and t_5, respectively, before the height were locked. These curves were not used when the model parameters in table 5.1 were determined. The experiments are further described in section 2.7.1.

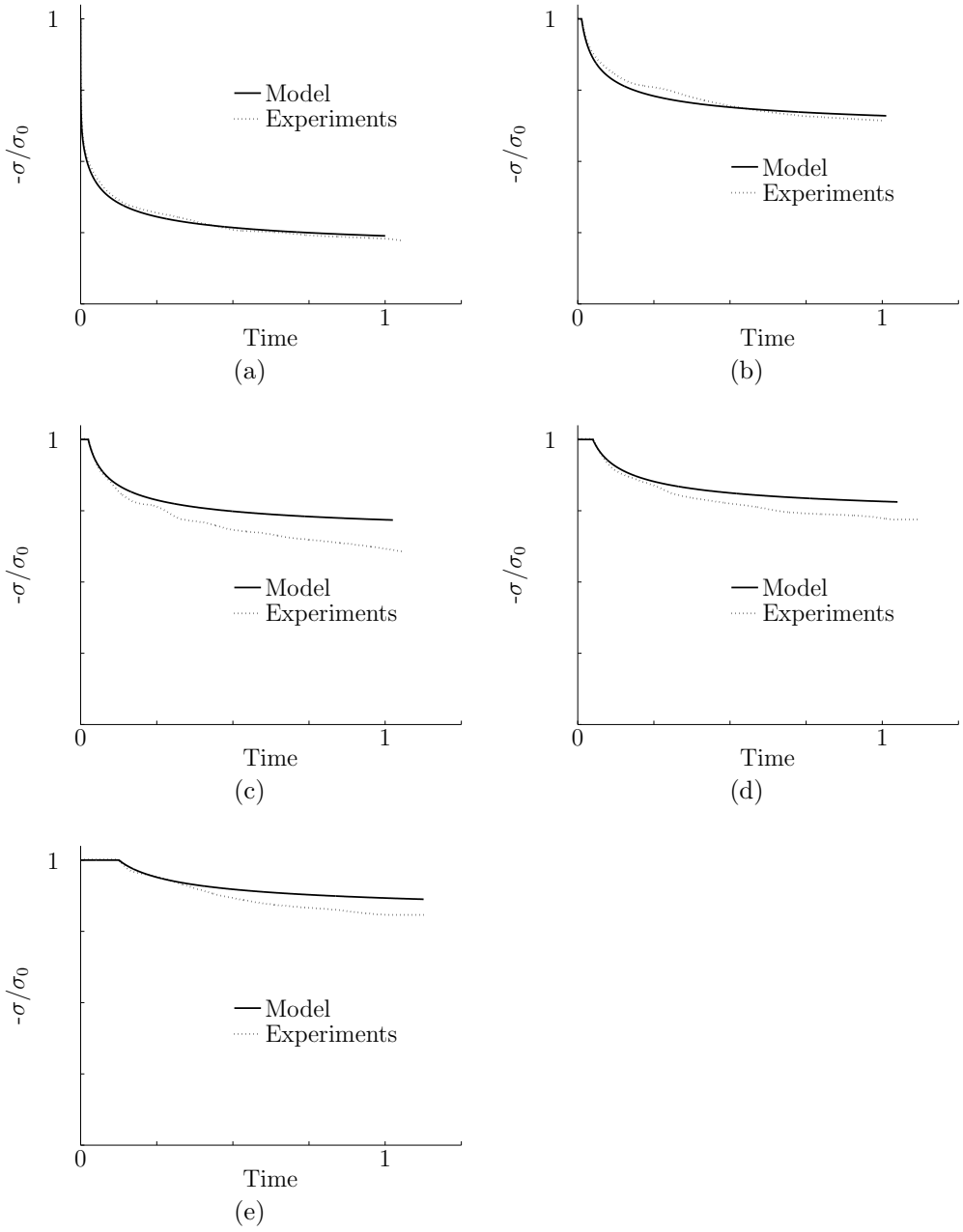

Figure 5.4: The graphs are showing the results from the 3-dimensional model compared to experimental data during a relaxation test with a duration of t_0 with the initial pressure. The pressure were held constant before locking the deformation for: (a) t_1, (b) t_2, (c) t_3, (d) t_4 and (e) t_5. Notice that the stress axis has been normalized using the normalization stress σ_0. The time axis is also normalized.

6 Abaqus implementation

The three dimensional constitutive model with isotropic creep presented in section 4 were implemented as an Fortran umat-subroutine[2] in the commercial finite element software Abaqus/Standard. In this section the modelling and some simulation results are presented. It should be noted that there are no experiments to which the results from the simulation can be compared.

6.1 Modelling

Simulations were made on a spacer component that acts as a support between the windings in a power transformer. In the simulation the spacer were compressed when a winding were pressed into the material in the Z-direction, see figure 6.1. The winding were displaced approximately 10 % of the thickness of the spacer. After the loading the displacement of the winding were fixed to simulate the response of the material during relaxation. Simulations were made at three different loading rates where the deformation step had a duration of: 10^{-1}, 10^{-3} and 10^{-5} hour. Because of symmetry only a quarter of the

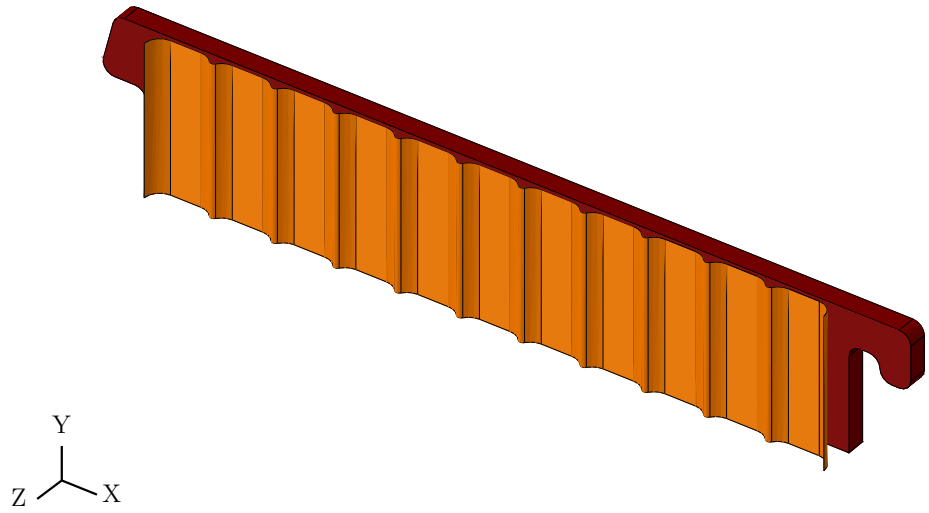

Figure 6.1: The figure is showing the spacer component (red part) and the part of a winding (orange part) that is pressed into the spacer during the simulation. The winding is displaced in the Z-direction.

[2]umat - user-defined material behaviour

spacer were regarded during the simulation, see figure 6.2. Symmetric boundary conditions were used on the symmetry planes, i.e. no displacement in the normal direction of the planes and no rotations around the normal direction of the planes. To fix the spacer in space one point in the center of the spacer on the symmetry XY-plane where locked in the X-direction. To reduce the

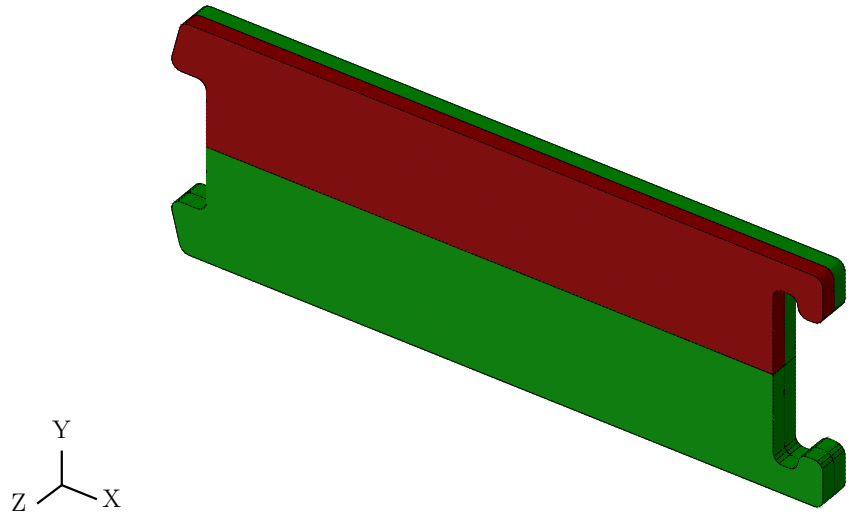

Figure 6.2: The figure is showing the spacer component that lies between the winding in a power transformer. The red part is showing the quarter of the spacer that is considered in the simulations.

computational time the winding were modelled as a analytical surface. The spacer where meshed with approximately 23600 C3D8 elements, which is a 8-node linear brick element. The meshed FE-model is shown in figure 6.3. The contact between the winding and the pressboard spacer were modelled using exponential pressure overclosure with 0.5 MPa contact pressure and 10^{-7} m clearance in the normal direction and penalty friction formulation, with friction coefficient 1, in the tangential direction, cf. [8].

6.2 Results

As mentioned before there are no experimental data to which the results can be compared. This means that one should not draw to large conclusions from the results presented in this section. However the results shows that the implemented model works from a computational point of view.

Figure 6.4 is showing the stress distribution in the deformed spacer when the loading is completed in 10^{-3} hour. The stress measure in the figure is von

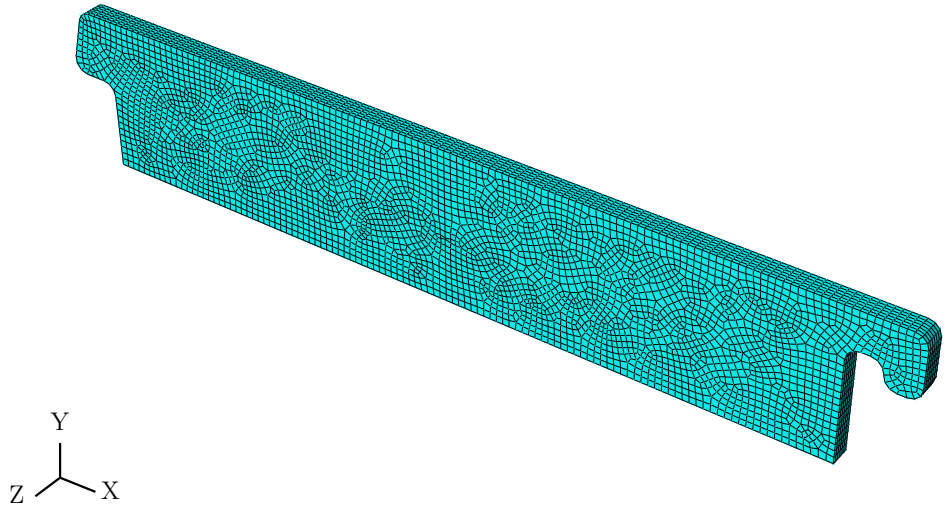

Figure 6.3: The figure is showing the meshed FE-model of the spacer component.

Mises effective stress. Some small areas are showing very high stresses, up to 1090 MPa, which is much higher than expected. This may be an effect of the mesh, the effected areas decreases with refined mesh. It may also be an effect of the contact between the spacer and the winding, very high stresses were encountered in some nodes on the contact surface of the spacer during the simulations. The high stresses may also be an effect of the assumption that the viscous parts are isotropic. As a consequence of this assumption the stress in MD and CD does not show any softening behaviour, see figure 4.1.

Figure 6.5 to 6.7 are showing the effective stress and the stress in Z-direction (33 direction) in the same element for the three loading rates. The stresses are calculated in the centroid of the element. The element is located on the surface of the spacer in one of the green areas shown in figure 6.4. The graphs in the figures are showing the stress in each of the three parts of the constitutive model as well as the total stresses, which are calculated according to

$$\sigma_{eff} = \sigma^{\infty}_{eff} + \sigma^{1}_{eff} + \sigma^{2}_{eff}; \quad \sigma_{33} = \sigma^{\infty}_{33} + \sigma^{1}_{33} + \sigma^{2}_{33} \tag{6.1}$$

The graphs, and mostly the graphs showing σ_{33}, are showing how the stress response of the three parts of the constitutive model is varying dependent of the loading rate. The greatest difference is found in the initial response. The initial stress after the loading is higher the higher loading rate and the stress relaxes more rapidly the higher the loading rate. The long term response of

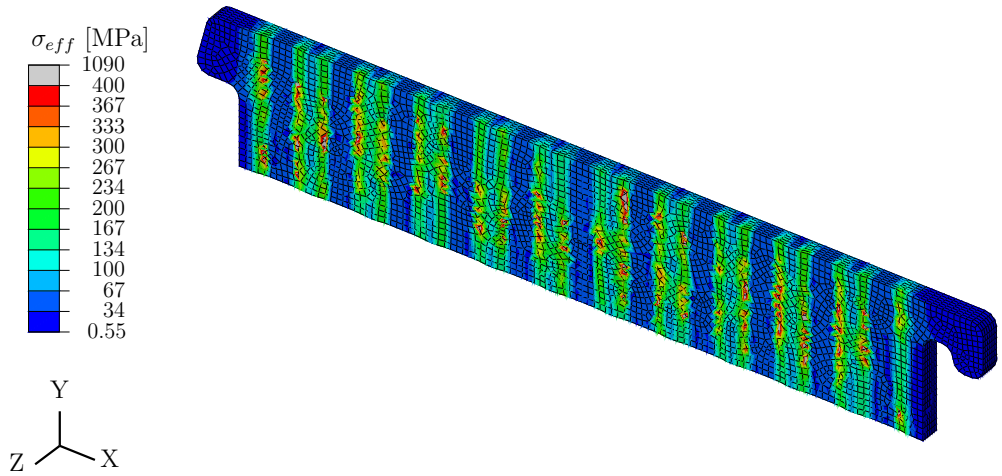

Figure 6.4: The figure is showing the stress distribution in the deformed spacer component just when the deformation is fixed after loading with the duration of 10^{-3} hour. The very high stress of upto 1090 MPa is probably an effect of the mesh and the contact between the spacer and the winding.

the material is unaffected by the loading rate. The graphs are showing that the initial relaxation is due to the relaxation of part number 3 in the model and the long term relaxation is due to the relaxation in part 2.

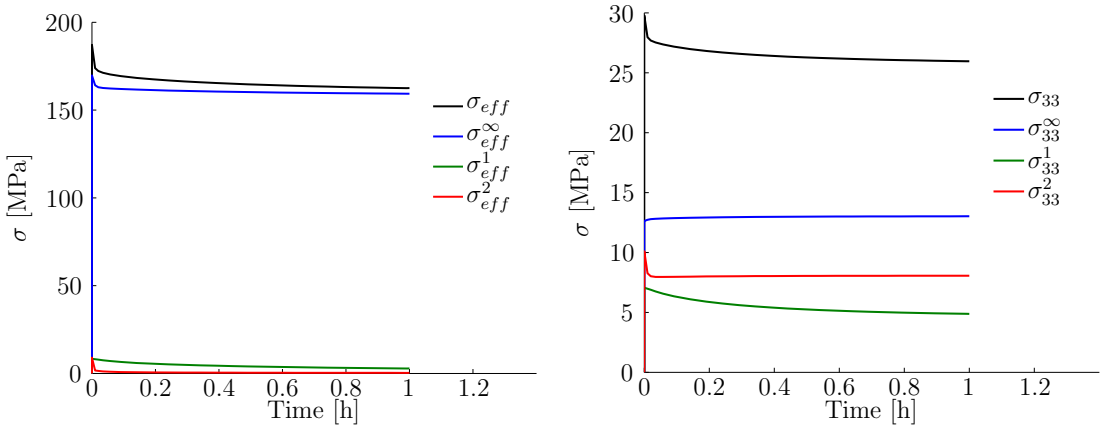

Figure 6.5: The graphs are showing the stress response in one element as a function of time when the loading duration is 10^{-5} hour. The graphs are showing the total stress as well as the stress in each of the three parts of the constitutive model. (a) is showing the effective stress and (b) are showing the stress in the Z-direction (33 direction).

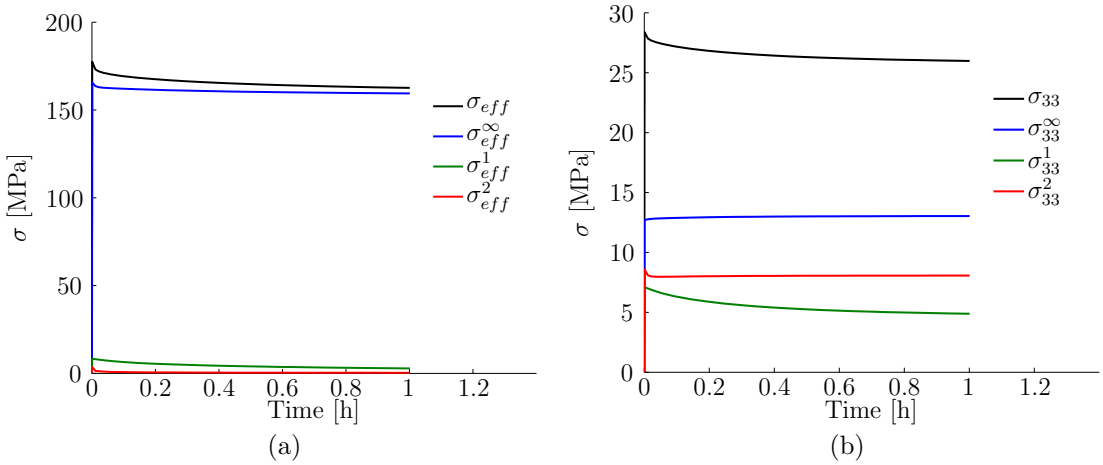

Figure 6.6: The graphs are showing the stress response in one element as a function of time when the loading duration is 10^{-3} hour. The graphs are showing the total stress as well as the stress in each of the three parts of the constitutive model. (a) is showing the effective stress and (b) are showing the stress in the Z-direction (33 direction).

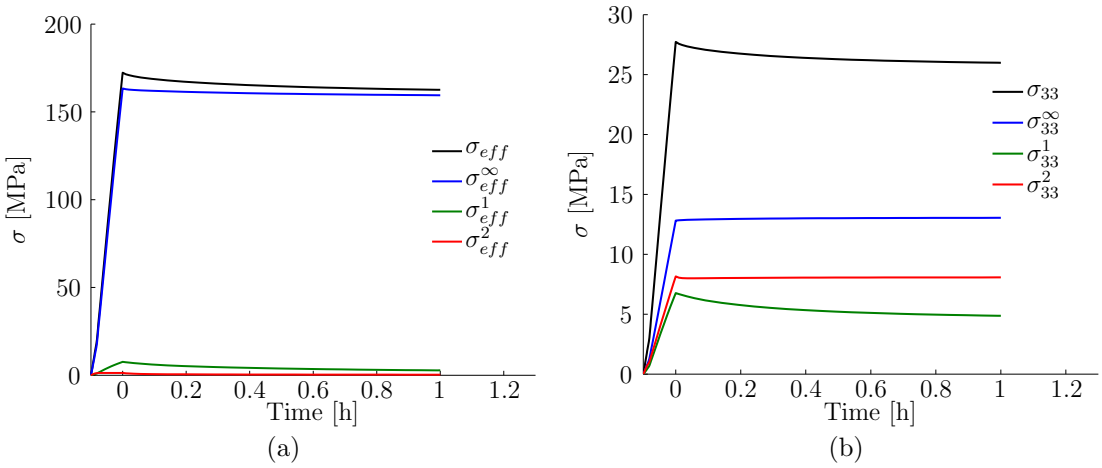

Figure 6.7: The graphs are showing the stress response in one element as a function of time when the loading duration is 10^{-1} hour. The graphs are showing the total stress as well as the stress in each of the three parts of the constitutive model. (a) is showing the effective stress and (b) are showing the stress in the Z-direction (33 direction).

7 Conclusions and discussion

In this section conclusions are drawn from the results of the experiments and the modelling done within this Master's thesis. Some proposals for further work is also presented.

7.1 Experiments

The experiments presented in section 2.1 shows some basic behaviours of pressboard such as anisotropy and some viscous effects displayed by the compression tests made at different loading rates. The experiments also revealed some difficulties regarding scatter between different test specimens. Three different actions where taken to reduce the scatter:

- Drying of the test pieces. Even though the test pieces where dried before shipping and even though they were stored wrapped in plastic it seems like the moisture content increased during storage. This is something too keep in mind because of that the moisture history of the material most likely will influence the mechanical behaviour.

- Straightening of the test pieces. The test pieces had an varying initial curvature which seems to influence the results of the tensile tests as test piece will be straightened out before being stretched. This makes the resulting experiment a combination of bending and uniaxial tensile.

- Using strain controlled loading instead of force controlled. The scatter decreased considerably when the loading where changed from force controlled to strain controlled, especially the scatter in the region of higher stress. This may very well be because of that the stress-strain curve levels out at higher stress.

This is showing on the difficulty to get good experimental result even from a such trivial experiment as a uniaxial tensile test.

7.2 Modelling

The essential results of the modelling is the results from the three dimensional models presented in sections 4.5 and 5.4. The model using isotropic creep response presented in section 4 shows good correlation to the out-of-plane relaxation experiments but no correlation to the uniaxial stress-strain curves outside the linear region. This is however no great surprise when the experiments shows relatively large differences in stiffness between the Z-direction

and the two other material directions. The model using anisotropic creep presented in section 5 capture the uniaxial stress-strain behaviour much better than the model with isotropic creep response while still capturing the out-of-plane relaxation behaviour well.

The difference in capability of capturing the relaxation behaviour between the two models is most likely to be found in the parameter mapping. With the "right" set of parameters for each model the relaxation response would probably be the same. However one could wish for an even better fit of the anisotropic model to the stress-strain curves, especially the out-of-plane compression curve. It may be possible to get a better fit with a different set of parameters or one may have to expand the model even further. The better fit of the in-plane behaviour of the model with anisotropic creep comes at the price of much larger computational work. This is mainly due to that the stress is solved from a coupled set of equations for anisotropic creep and reduced to a single scalar expression for the isotropic creep. It was also found that to get the model with anisotropic creep to convergence the length of the time step had to be shorter than for the model with isotropic creep which leads to even more computational work.

One should keep in mind that one of the assumptions that the models are based on is that the creep strains are assumed to be incompressible, i.e. $\varepsilon_{ii} = 0$. This is an assumption that is open for discussion but without any experimental data this assumption can be said to be as good or bad as any other.

The results from the simulations made in Abaqus with the model with isotropic creep presented in section 6.2 shows how the different parts of the constitutive model responds at different loading rates. This could also be an explanation to the need of extending the constitutive model with one extra viscous element in order to capture the behaviour from the in-plane tensile tests. These tests are made with very short duration in comparison with the relaxation tests and so one needs an additional time-scale to describe both sets of experiments with the same model. This is something that were observed during initial attempts to fit the model with anisotropic creep to both types of experiments without extending the model with an extra viscous part. Without extending the model did fit well to either the short term uniaxial tensile and compression test or the long term relaxation test.

7.3 Further work

Through the experimental work and the modelling carried out in this Master's thesis one has just scratched the surface of the characterization of pressboard. To get more understanding of the behaviour of pressboard more ex-

periments such as uniaxial tensile and compression tests at different loading levels and loading rated, relaxation experiments at different loading levels and shear tests has to be carried out. There are no experiments that shows anything about the Poission's ratios or the behaviour during shear of pressboard. An other aspect is temperature and moisture. All experiments in this thesis has been made at room temperature and with test pieces with more or less unknown moisture content. It is an more than reasonable assumption that the behaviour is dependent on both temperature and moisture content. Furthermore there are no experiments showing remaining deformation due to plasticity.

A first continuation may be to extend the model to include large deformations. With more experimental data to base further modelling on the model could be remade to also include temperature dependence and plasticity.

References

[1] Prevost, T. A. and Oommen, T. V. (2006). *Cellulose insulation in oil-filled power transformers: Part I - history and development*. Electrical Insulation Magazine, IEEE, 22, 28-35.

[2] Ottosen, N. S. and Ristinmaa, M. (2005). *The Mechanics of Constitutive Modeling*. Elsevier.

[3] CEI/IEC 60641-2:2004. (2004). *Pressboard and presspaper for electrical purposes – Part 2: Methods of tests*. International Electrotechnical Commission. Geneva.

[4] Böiers, L-C. (2010). *Mathematical Methods of Optimization*. Studentlitteratur. Lund.

[5] Ottosen, N. S. and Petersson, H. (1992). *Introduction to the Finite Element Method*. Prentice hall.

[6] Wallin, M. and Ristinmaa, M. (2005). *Deformation gradient based kinematic hardening model*. International Journal of Plasticity, 21, 2025-2050.

[7] Kulkarni, D. V., Tortorelli, D. A. and Walling, M. (2007). *A Newton–Schur alternative to the consistent tangent approach in computational plasticity*. Computer methods in applied mechanics and engineering, 196, 1169-1177.

[8] Huand, H. and Nygårds, M. (2010). *A simplified material model for finite element analysis of paperboard creasing*. Nordic Pulp and Paper Research Journal, 25, 505-512.

A Results from experiments

A.1 Effect of moisture

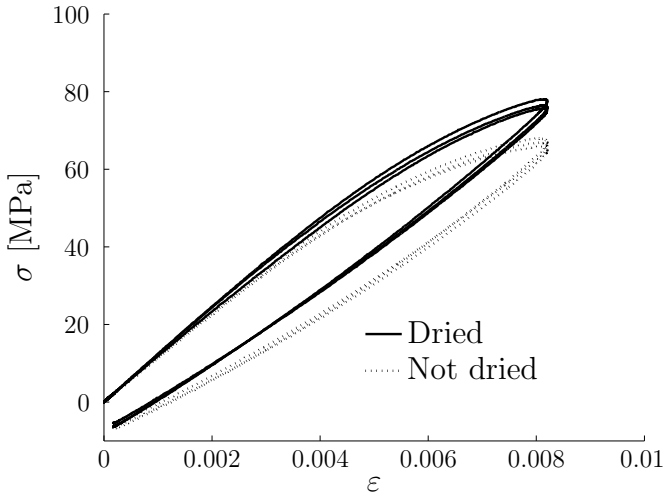

Figure A.1: The graph shows how the moisture content of the material affects the stiffness. The samples labeled "Not dried" has been stored wrapped in plastic but not dried after delivery. The test pieces were loaded using a sinus shaped strain curve with a constant frequency of 0.1 Hz.

A.2 Initial curvature

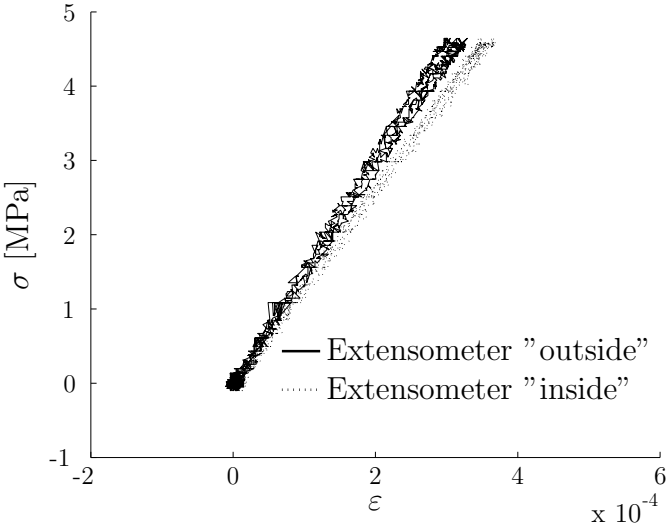

Figure A.2: The graph shows how the strain differs between the two sides of the test piece due to the initial curvature. The solid lines is showing the strain when the extensometer is fitted on the "outside" of the curvature and the dashed lines the strain measured on the "inside". The test piece were dried before the test. The tests were made using a sinus shaped loading curve with a constant frequency of 0.1 Hz.

A.3 Loading until fracture

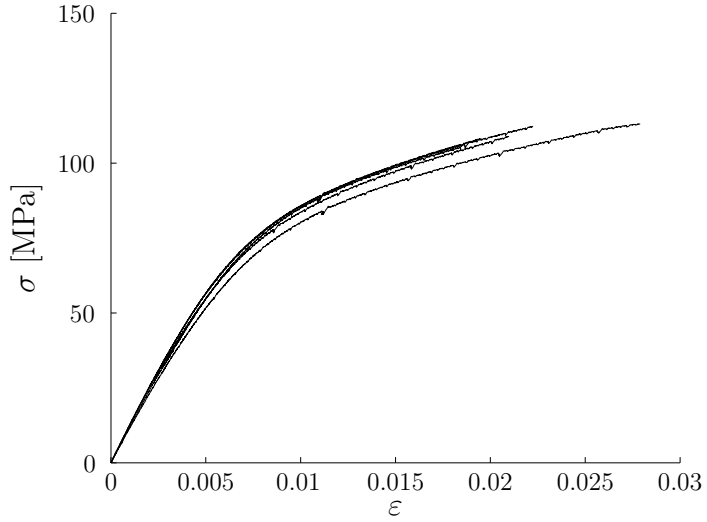

Figure A.3: Uniaxial stress-stain curves for loading until fracture in the CD-direction using a constant rate of displacement of 6 mm/min. The test pieces were not dried before the test.

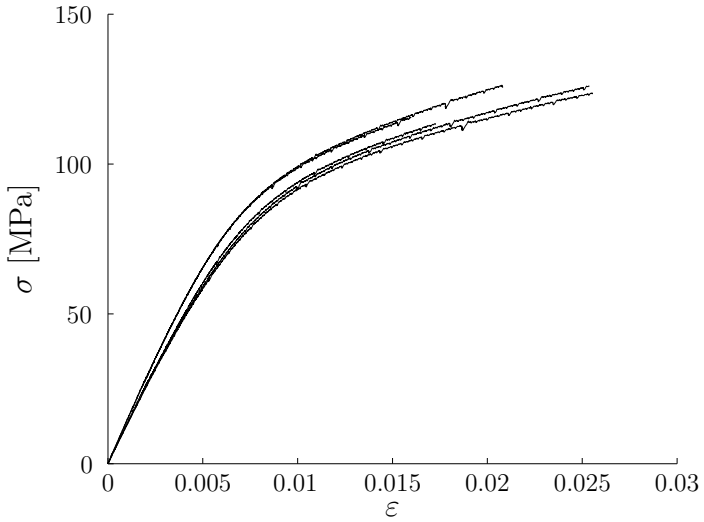

Figure A.4: Uniaxial stress-stain curves for loading until fracture in 45 degrees to the MD-direction using a constant rate of displacement of 6 mm/min. The test pieces were not dried before the test.

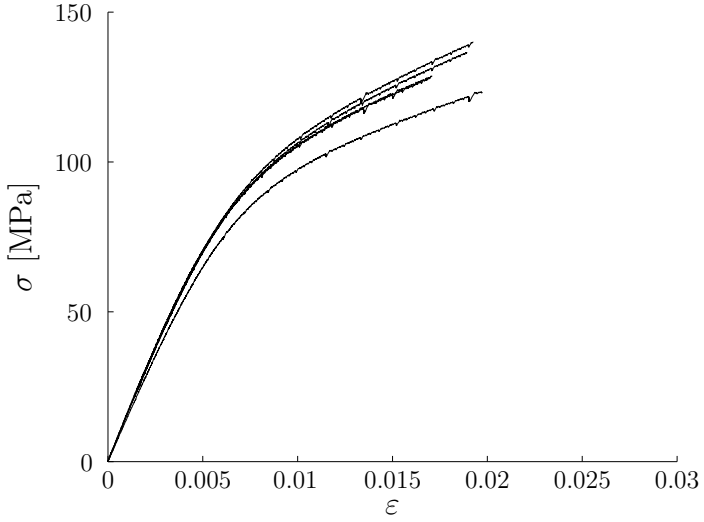

Figure A.5: Uniaxial stress-stain curves for loading until fracture in the MD-direction using a constant rate of displacement of 6 mm/min. The test pieces were not dried before the test.

A.4 Cyclic tensile testing

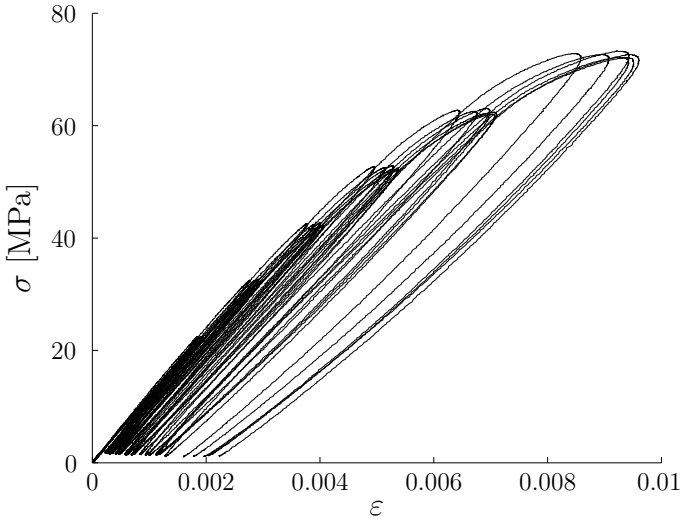

Figure A.6: Uniaxial stress-strain curve with load controlled cyclic loading/unloading in the CD-direction. The test pieces were not dried before the test. The test pieces were loaded using a sinus shaped loading curve with a constant frequency of 0.1 Hz.

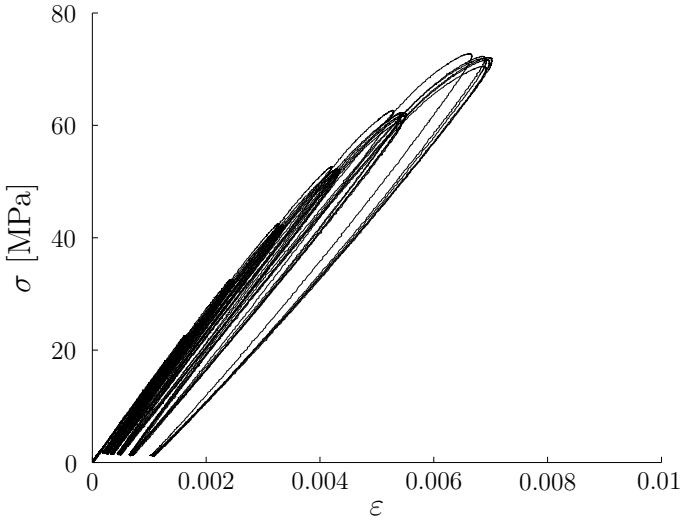

Figure A.7: Uniaxial stress-strain curve with load controlled cyclic loading/unloading in 45 degrees to the MD-direction. The test pieces were not dried before the test. The test pieces were loaded using a sinus shaped loading curve with a constant frequency of 0.1 Hz.

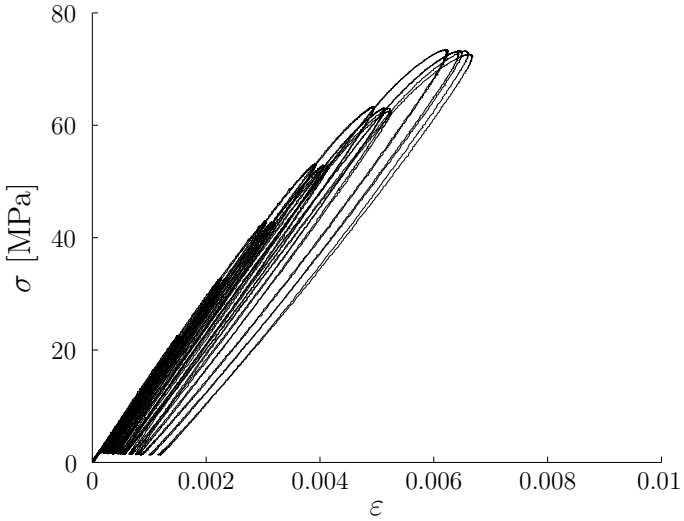

Figure A.8: Uniaxial stress-strain curve with load controlled cyclic loading/unloading in the MD-direction. The test pieces were not dried before the test. The test pieces were loaded using a sinus shaped loading curve with a constant frequency of 0.1 Hz.

A.5 Strain controlled loading

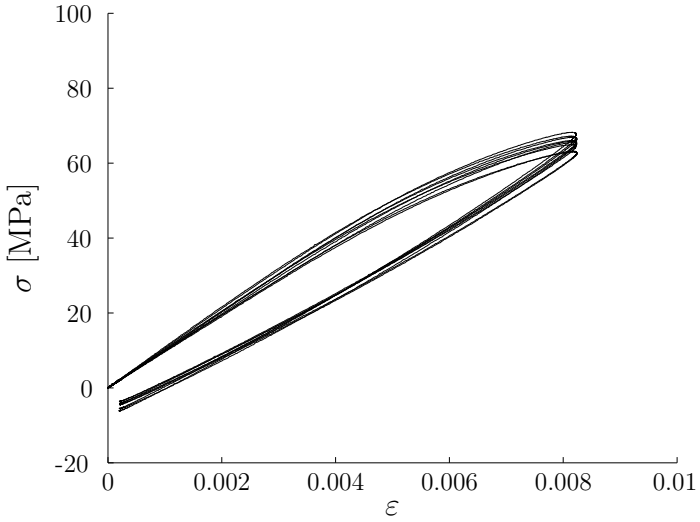

Figure A.9: Uniaxial stress-strain curve with strain controlled cyclic loading/unloading in the CD-direction. The test pieces were dried before the test. The test pieces were loaded using a sinus shaped strain curve with a constant frequency of 0.1 Hz.

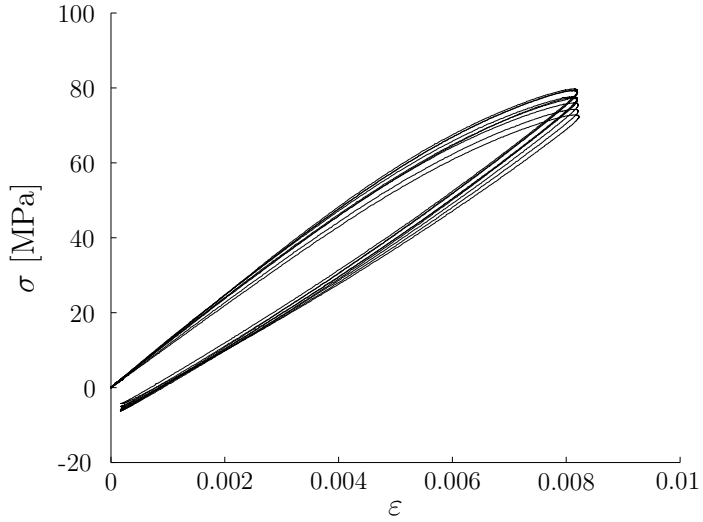

Figure A.10: Uniaxial stress-strain curve with strain controlled cyclic loading/unloading 45 degrees to the MD-direction. The test pieces were dried before the test. The test pieces were loaded using a sinus shaped strain curve with a constant frequency of 0.1 Hz.

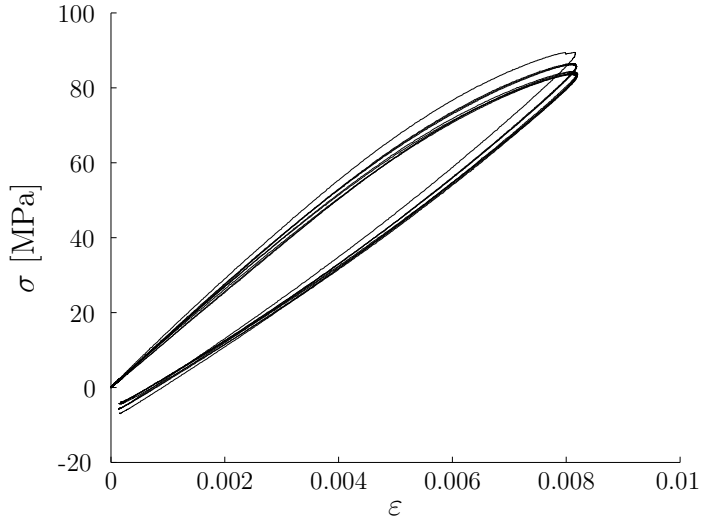

Figure A.11: Uniaxial stress-strain curve with strain controlled cyclic loading/unloading in the MD-direction. The test pieces were dried before the test. The test pieces were loaded using a sinus shaped strain curve with a constant frequency of 0.1 Hz.